PLASMA FLOW CONTROL FOR DISTORTION TOLERANT FANS WITH AIRCRAFT BOUNDARY LAYER INGESTION

By

TYLER ZIMBELMAN

Bachelor of Science Biosystems Engineering

Oklahoma State University

Stillwater, Oklahoma

2013

Submitted to the Faculty of the
Graduate College of
Oklahoma State University
in partial fulfillment of
the requirements for
the Degree of
MASTER OF SCIENCE
May, 2018

PLASMA FLOW CONTROL FOR

DISTORTION TOLERANT FANS WITH AIRCRAFT

BOUNDARY LAYER INGESTION

Thesis Approved:

Dr. Kurt Rouser

Thesis Advisor

Dr. Jamey Jacob

Dr. Richard Gaeta

ACKNOWLEDGMENTS

First, I would like to thank my family for being my biggest supporters. My wife Kelley Zimbelman, mother Stephanie Zimbelman, and sister Abby Zimbelman. I would also like to thank my advisor, Dr. Kurt Rouser, for his teaching and guidance throughout this project, as well as the rest of my committee, Dr. Jamey Jacob and Dr. Richard Gatea, for their time and feedback during my thesis presentation. Next, I would like to thank my friends Nick Lucido, Alvin Ngo, Kylar Moody, and Real KC for the continued support in the lab during manufacturing and testing.

Acknowledgements reflect the views of the author and are not endorsed by committee members or Oklahoma State University.

Name: Tyler Zimbelman

Date of Degree: May, 2018

Title of Study: PLASMA FLOW CONTROL FOR DISTORTION TOLERANT FANS WITH AIRCRAFT BOUNDARY LAYER INGESTION

Major Field: Mechanical and Aerospace Engineering

Abstract:

Recent efforts to reduce commercial transport aircraft drag include embedding an aft-mounted engine into the airframe in order to fill the vehicle wake with engine exhaust, consequently reducing fuel consumption. Embedded engines can provide substantial improvements compared to conventional wing-mounted engines by generating thrust with lower-momentum boundary layer ingestion; however, the propulsion system must be capable of performing effectively in a highly distorted flow field. An active flow control technique for reducing distorted boundary layer flow entering an embedded duct is evaluated. Plasma flow control is proposed to reduce flow field distortion. Plasma actuators have previously demonstrated capability to manipulate boundary layer growth by imparting a body force on the flow near the surface, increasing momentum. Multiple variables were evaluated in this study to determine potential flow field improvement, including actuator location, frequency, and power input. Tests were conducted in a low-speed, open-loop wind tunnel with a traverse-mounted pitot-static probe to determine dynamic pressure at an embedded duct exit plane. A single-dielectric-barrier-discharge plasma actuator was tested over a range of wind tunnel speeds at different locations relative to an embedded duct inlet. The local operating Reynolds number due to ramp surface length ranged from 1 to 3 million. The test article was a notional boundary layer ingestion ramp and contraction duct having a 1.25:1 area contraction ratio and 10-inch circular, exit diameter. The duct geometry was a modified NACA 0012 airfoil, and the plasma actuator consisted of two copper electrodes separated by a 0.024-inch thick Mica dielectric barrier. A non-dimensional distortion intensity coefficient was used to evaluate plasma actuator performance. Furthermore, qualitative assessments of velocity contour plots are presented. Results reveal the effectiveness of plasma flow control to manipulate distortion intensity.

TABLE OF CONTENTS

LIST OF FIGURES

LIST OF TABLES

CHAPTER I

INTRODUCTION

1.1. Motivation

An important objective of future aircraft concepts is to reduce fuel burn for commercial transport, and one novel technology currently being researched is boundary layer ingesting (BLI) propulsion systems. Figure 1 illustrates a BLI aircraft concept being evaluated in NASA Glenn's wind tunnel. The concept employs two aft turbofan engines mounted flush with the top of the fuselage [1]. Conventional aircraft utilize a wing-mounted engine to provide uniform flow at the inlet duct. With BLI aircraft, the engine is mounted closer to the aircraft body and a portion of the fuselage boundary layer is ingested through the propulsor. Ingesting lower momentum flow along the surface of the boundary layer posi-

Figure 1: Boundary Layer Ingestion Aircraft Concept. [1]

tively affects propulsive efficiency, the primary mechanism by which fuel consumption is reduced for BLI aircraft. Propulsive efficiency is defined as

$$\eta_{\mathrm{p}} = \frac{2}{1 + V_9/V_0} \tag{1}$$

and increases as the exit velocity (V_9) approaches the inlet velocity(V_0).

Plas et al. showed that the percentage of BLI increases, the propulsive efficiency increases [1]. Ingesting lower velocity aircraft boundary layer reduces exit velocity at a faster rate than inlet velocity. This improved propulsive efficiency is seen in fuel burn savings up to 8% [2]. This is true for larger aircraft, but also for smaller unmanned aircraft systems (UAS) that employee boundary layer ingestion. However, in order to realize the benefits of BLI, the propulsion system must be capable of operating in a high-distortion flow field. Propulsors designed to operate in BLI conditions often experience distorted flow, negatively affecting aircraft performance and efficiency. Distorted flow may affect the relative angle of attack observed by the fan blade, creating flow separation, vibration, and blade stall. Two ways for reducing distortion are affecting the flow over the fan or compressor blade, or by affecting the flow upstream of the inlet. This study will evaluate the potential of affecting the flow on the ramp leading to the inlet duct and not on the blade.

Flow control methods have shown the capability to manipulate boundary layer and distorted flow, and are generally categorized as passive or active. A flow control device can be considered passive or active. Passive flow control typically encompasses surface modifications that cannot be manipulated on and off, even when unwanted or hurting performance. Examples include vortex generators, boundary layer trips, or dimples on a golf ball. Alternatively, active flow control induces higher momentum to the flow and has the ability to be manipulated during operation. The ability to manipulate the device during operation makes active flow control advantageous for use in this study.

Plasma actuators are one example of an active flow control method previously shown to affect boundary layer flow [3]. Corke et al. detailed the principles and setup of a plasma flow control device, which included two copper electrodes separated by a di-

electric barrier, one exposed to ambient air on the suction surface and one encapsulated on the pressure surface[4]. High voltage is applied to ionize surrounding air, generating a body force that imparts momentum to the flow. For this study, the use of plasma flow control will be evaluated for manipulating distorted flow in an embedded duct.

1.2. Goals and Objectives

The goal of this work is to evaluate the use of plasma flow control for manipulating distorted flow through an embedded duct. A representative BLI test arrangement will be designed, manufactured, and characterized to gain a thorough understanding of distortion created by geometry and BLI effects. Multiple concepts will be explored employing plasma flow control on BLI configurations; and a plasma actuator will be designed and manufactured. Finally, an evaluation will be performed to determine the effectiveness of a plasma actuator to manipulate distortion in a representative BLI arrangement. With this knowledge, improvements can be made to optimize a method for flow control on BLI propulsion systems.

1.3. Thesis Outline

Background and relevant literature on BLI, flow control, and plasma flow control specifically are provided in Chapter 2. Chapter 3 contains a description of the facilities and presents the development of the BLI test arrangement used for this study and the tests conducted. Chapter 4 contains the results from testing the various wind tunnel speeds, actuator locations, and actuator frequencies on a representative BLI arrangement. Chapter 5 presents the method for uncertainty analysis and the corresponding values relative to wind tunnel freestream velocity and duct centerline velocity. Conclusions and recommendations for future work are provided in Chapter 6.

CHAPTER II

BACKGROUND

2.1. Boundary Layer Ingestion Engines

Boundary layer ingestion engines have been proposed as a way to increase range and endurance for commercial aircraft. This is done by reducing the propulsor power required by the aircraft and increasing the propulsive efficiency [5]. Reducing required propulsor power is achieved by filling the wake deficit created by the aircraft fuselage with higher momentum jet exhaust. Figure 2 illustrates the momentum profile of BLI propulsion systems compared to conventional wing-mounted propulsion systems. Conventional propulsion systems without BLI consist of airframe drag, momentum deficit in the downstream wake, and propulsor thrust, excess momentum in the propulsor exhaust. With BLI, a portion of the fuselage boundary layer is ingested through the propulsor, reducing the momentum deficit behind the aircraft and excess propulsor kinetic energy. Many BLI concepts

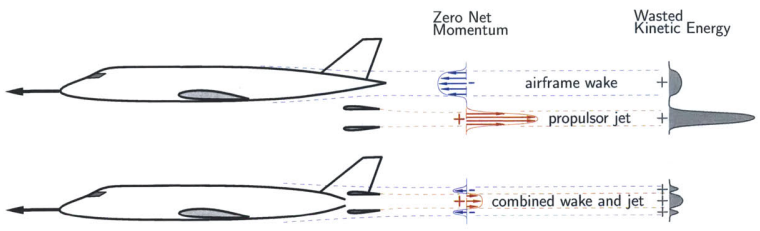

Figure 2: Conventional aircraft wake profile compared to BLI aircraft. [6]

have been proposed in order to improve fuel efficiency and reduce noise, and conceptual studies have been performed to evaluate the performance of BLI systems. One of the earliest was Smith who evaluated benefits of wake ingesting propulsors and created a method to estimate the amount of propulsive power saved when embedding the propulsive flow in the viscous wake of a body[7]. With the propulsive power reduced and increased propulsive efficiency due to embedding the engine, as much as 20% reduction in fuel burn was estimated. Another concept is a blended wing body(BWB) aircraft that was evaluated to determine potential improvements by integrating engine inlets into an aircraft fuselage and applying flow control methods to improve flow quality[8–10]. Figure 3 depicts a BWB concept to improve fuel efficiency and reduce emissions. The BWB concept integrated multiple next-generation turbofans in the top, aft end of the aircraft fuselage. The most significant reduction in fuel burn was estimated at 10% with the addition of flow control methods to reduce the offset of the embedded inlet duct. The D8 Double Bubble is another example of a BLI aircraft concept to reduce fuel burn and noise[6, 11, 12]. Figure 4 depicts the D8 concept that utilizes two turbofan engines embedded at the aft end, flush with the top aircraft fuselage in order to ingest 40% of the boundary layer flow. Engine weight

Figure 3: Illustration of a blended wing body aircraft concept. [9]

Figure 4: Illustration of the D8 Double Bubble boundary layer ingestion aircraft concept. [13]

is reduced by shortening engine inlet length due to the fuselage developing the upstream flow at the fan. Estimated results show as much as 36% improvement in fuel efficiency compared to conventional aircraft. Plas et. al has also demonstrated as percentage of BLI increases, the propulsive efficiency increases due to a reduction in propulsor exit velocity, consequently reducing fuel consumption[1]. However, in order to realize the benefits of BLI, the propulsion system must be capable of operating in a high distortion flow field. A basic understanding of boundary layer theory is necessary before determining methods for improving BLI operating conditions.

2.2. Boundary Layer Theory

A boundary layer is a thin, viscous layer of fluid near a solid surface contacting moving flow, shown in Figure 5. Fluid traveling in a positive x direction at a freestream velocity(u_∞) passes over a solid surface. Assuming a "no-slip" condition at the wall, velocity is zero and varies ($u(y)$) from zero at the wall to u_∞ at the boundary layer. Boundary layer thickness(δ) increases as x increases, however, δ is an artificially introduced point where velocity reaches 99% of u_∞. The primary parameter for viscous flow is the dimen-

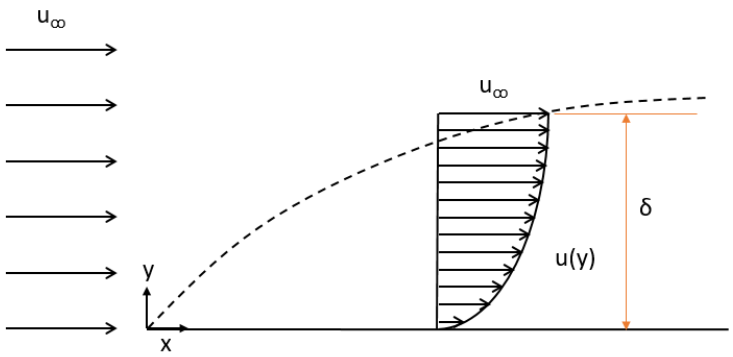

Figure 5: Boundary layer over a flat plate.

sionless Reynolds number (Re)[14]. Reynolds number is defined as

$$Re_L = \frac{\rho \times U \times L}{\mu} \tag{2}$$

where ρ is the fluid density, U is the relative velocity, L is the characteristic length, and μ is the dynamic viscosity. Reynolds number is sensitive to fluid property changes, and manipulating Re will have a significant impact on flow.

2.2.1. Laminar and Turbulent Boundary Layer

Laminar flow is present when layers of fluid moving at different velocities do not exchange fluid particles perpendicularly[15]. Boundary layer flows with a Reynolds number between 1000-10^6 are most likely laminar. Reynolds number greater than 10^6, the flow is considered turbulent, or highly random, fluctuating flow causing particle mixing perpendicular to the flow path. It is important to understand the differences between laminar and turbulent flows as they behave in the boundary layer. Figure 6 illustrates the difference in velocity profile shape between laminar and turbulent boundary layers. A laminar boundary layer initially grows over a body surface and as the distance traveled by the flow increases from the leading edge, the laminar boundary layer is replaced by a more rapidly growing and thicker turbulent layer[16]. The region flow changes from laminar to turbulent is considered laminar to turbulent transition. Transition can occur from a laminar to turbulent

boundary layer many different ways: surface roughness, curvature, and temperature as well as pressure gradients and increasing/decreasing Reynolds number[16].

2.2.2. Attached and Separated Boundary Layers

Flow over a smooth surface that does not experience an adverse pressure gradient is commonly referred to as attached boundary layer flow. An adverse pressure gradient can occur when velocity does not remain positive in the axial direction, causing recirculation or reverse flow. Flow that experiences an adverse pressure gradient over a specific distance may experience a reduction in velocity near the surface, causing recirculation and separated flow. Figure 7 illustrates the concept of flow separation over a varying surface geometry. The adverse pressure gradient near the surface alters the streamlines of the bulk flow and prevents attachment from continuing. Separated flow may contain a corresponding non-dimensional shedding frequency known as the Strouhal number (St). Strouhal number is defined as

$$St = \frac{f \times D}{U} \tag{3}$$

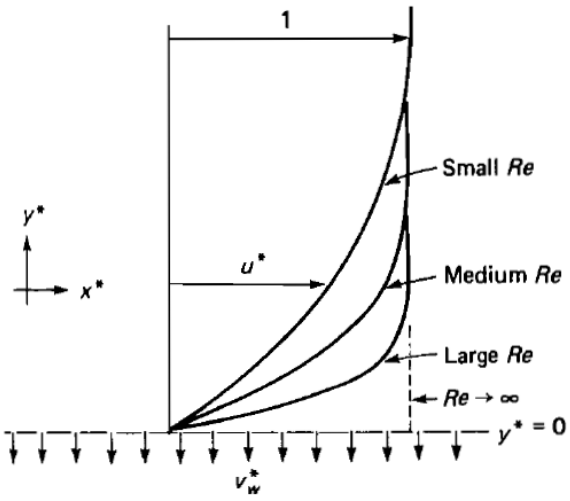

Figure 6: Boundary layer velocity profiles as a function of Re. [14]

For Re between 10 and 10^5, Strouhal number is approximately equal to 0.2. Determining the shedding frequency within the flow allows distortion

2.3. Engine Inlet Distortion

Jet engines pull air through an inlet, compress it to high pressures, mix it with fuel for combustion, expand through a turbine to extract power, and send the exhaust out a nozzle to produce thrust. The entrance of the engine directs and prepares the flow before the fan face, comprised of rotor blades having airfoil geometries producing lift by changing the direction of the flow. Figure 8 illustrates the basic geometry and forces of a cross-sectional cut fan blade. The incoming air has an associated incidence angle relative to the airfoil fan blade and because of this relationship; jet engines are very sensitive to non-uniform flow. Non-uniform flow or distorted flow negatively affects jet engine performance and, more importantly, reduces the fan and compressor stable flow range[17–21]. The most common types of distorted flow at the inlet are total pressure distortion, total temperature distortion, and swirl distortion, which may form by different means[22].

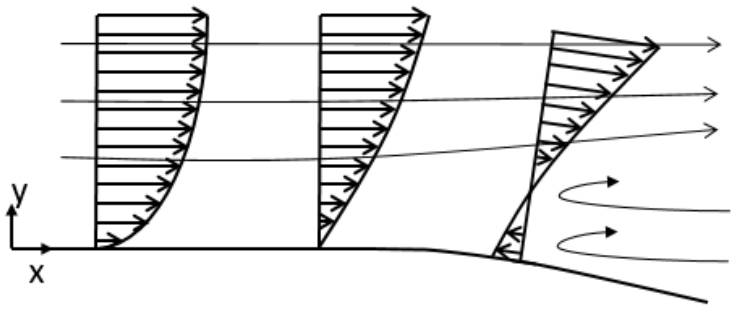

Figure 7: Illustration of changing velocity profiles as flow begins to reverse direction and separate in the boundary layer.

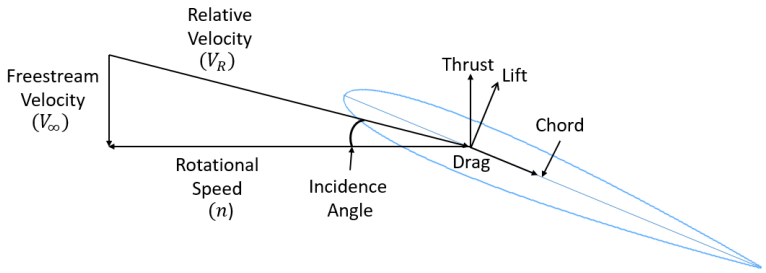

Figure 8: Two-dimensional airfoil geometry illustrating forces and incidence angle.

2.3.1. Total Pressure Distortion

Total pressure distortion can happen different ways, such as boundary layer ingestion through embedded inlet ducts, high angle of attack operation, or side winds. Figure 9 illustrates total pressure distortion over a cross-sectional measurement plane inside an embedded engine inlet. From previous boundary layer theory, velocity at the surface is zero and boundary layer flow has lower momentum. Lower velocity equates to lower kinetic energy, $(1/2)\rho V^2$, which is the dynamic component of pressure. As dynamic pressure decreases and static pressure remains constant, total pressure decreases producing a total pressure distortion that may not be mostly symmetric as Figure 9 appears. It is helpful to

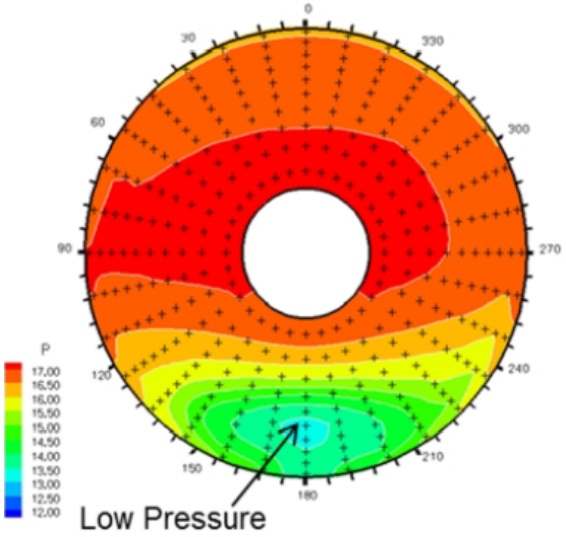

Figure 9: Inlet distortion for an embedded engine. [23]

conceptually break total pressure distortion into radial and circumferential components, illustrated in Figure 10, in order to evaluate both individually[19]. Radial distortion intensity is defined as

$$\text{Radial Distortion Intensity} = \frac{\Delta P_R}{P} = \frac{PFAV - PAV_i}{PFAV} \tag{4}$$

where PFAV is the face-average pressure and PAV_i is ring average pressure, and normalizing the difference yields radial distortion intensity[24]. Radial distortion will be discussed only briefly as circumferential distortion often produces the larger impact on performance and makes up the more significant contribution to overall distortion[19]. Circumferential distortion is defined as

$$\text{Circumferential Distortion Intensity} = \frac{\Delta P_C}{P} = \frac{PAV_i - PAVLOW_i}{PAV_i} \tag{5}$$

where PAV_i is ring average pressure and $PAVLOW_i$ is an integral value taken over an angular region where pressure is lower than PAV_i and values are obtained using linear interpolation of pressure for an instrument ring[24]. Normalizing the difference ofPAV_i and $PAVLOW_i$ by PAV_i yields circumferential distortion intensity.

$$PAV_i = \frac{1}{360}\int_0^{360} P(\theta)_i \, d\theta \tag{6}$$

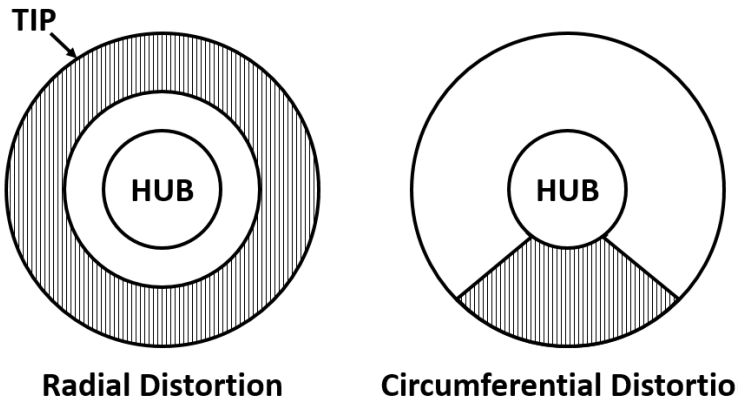

Figure 10: Total Pressure Distortion Components Radial(left) and Circumferential(right).

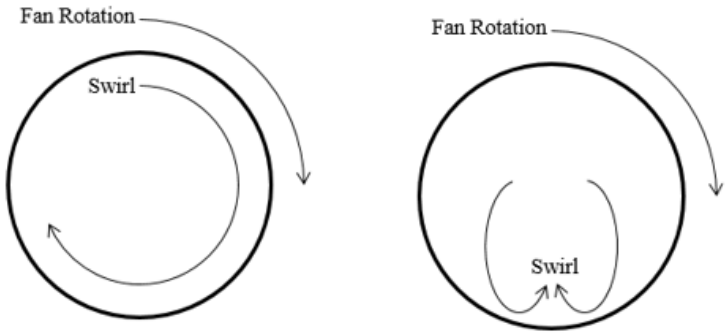

Figure 11: Two types of swirl: bulk swirl(left) and paired swirl(right).

$$PAVLOW_i = \frac{1}{\theta_i^-} \int_{\theta_i}^{0} P(\theta)_i \, d\theta \tag{7}$$

2.3.2. Total Temperature Distortion

Total temperature distortion takes place when there is a nonuniform total temperature profile present[25]. An example case where total temperature distortion occurs would be ingesting hot exhaust gases from weapons after firing. Total temperature distortion will not be evaluated in this study.

2.3.3. Swirl Distortion

Swirl distortion is nonuniform flow angularity, typically present in embedded and boundary layer ingestion inlets. Swirl can be broken into two components, bulk and paired swirl. Both types of swirl are shown in Figure 11. Bulk swirl at the engine inlet is generated by the rotation of turbomachinery downstream, and direction of rotation can be the same or opposite of the turbomachinery. Paired swirl is generated by the geometry of the embedded engine inlet, and can be symmetric or offset. Swirl distortion effectively changes the incidence angle experienced by the fan blade, causing stall and flow separation over the aft blade section. Endwall losses or ”horseshoe vortices have been researched previously due to the contribution to swirl distortion for embedded ducts[26–28]. The ability to control

swirl, as well as other types of distortion ingested by embedded engines may significantly improve performance and operability.

2.4. Flow Control

Flow control is the ability manipulate a flow field to yield a desired change[29]. Example outcomes of flow control techniques include, but are not limited to: reduced separation and drag reduction, increased lift, and improved mixing. Gad-el-hak et al. reviewed a broad range of flow control techniques, which can be divided into passive and active methods[29]. Figure 12 depicts some examples of passive flow control methods. Passive flow control typically consists of surface modifications that cannot be manipulated on and off. Examples include vortex generators, boundary layer trips, or dimples on a golf ball. Active flow controls have the ability to be turned off during operation when unneeded, and often have the ability to be tuned to different flow conditions. Figure13 illustrates some examples of active flow control techniques.

2.4.1. Passive Flow Control

Passive techniques are typically more durable due to being integrated or built into the existing surface, making passive devices ideal for harsh operating conditions. Several passive flow control methods exist to affect a flow field. Previous researched has evaluated the use of surface modifications as a means of control flow. One surface treatment

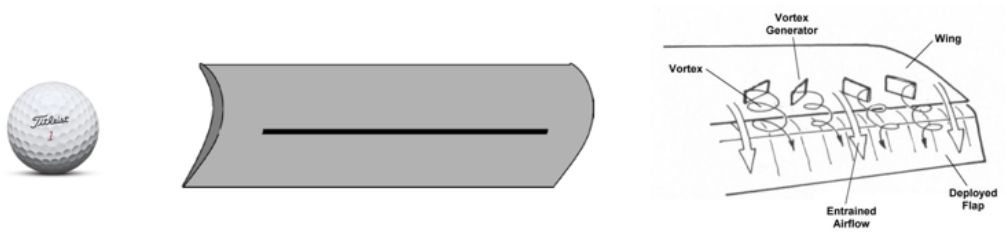

Figure 12: Examples of passive flow control devices: golf ball dimples(left), boundary layer trip(middle), vortex generators(right). [30–32]

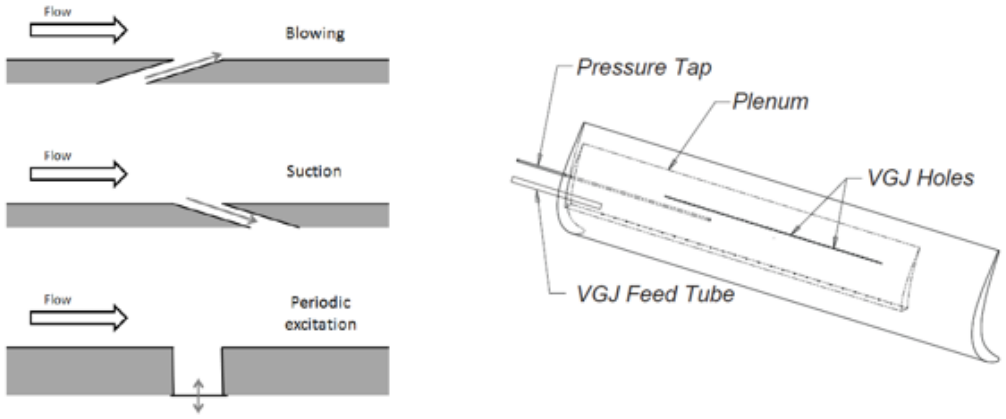

Figure 13: Examples of active flow control devices: pneumatic actuators(left) and vortex generator jets(right). [33, 34]

is protruding geometry to trip the flow upstream of the boundary layer separation. Zhang et al. experimentally investigated the use of surface trips on turbine blades to reduce profile losses[35]. Cylindrical wires and rectangular bars were used as surface trips for the experiments. Using a trip to cause momentum entrainment from the freestream down to the surface successfully reduced the profile loss at every Reynolds number tested. Zhang et al. further investigated this passive technique, but also included a comparison between surface trips and vented jet blowing at low Reynolds number regimes[36]. Air was vented from pressure side to suction side on the turbine blade to control the boundary layer development. This technique demonstrated the ability to reduce the profile losses below that of a smooth surface, but was not as effective as a boundary layer trip. Lin et al. evaluated large eddy breakup devices, as well as vortex generators[37]. Vortex generators proved effective at manipulating separation, but effectiveness relied on mounting location in relation to the separation bubble and vortex generator geometry. The ability to manipulate flow using triangular vortex generators was investigated by Chang and Gamerdinger et al.[38, 39]. Gamerdinger et al. determined triangular vortex generator devices had the ability to decrease boundary layer separation due to shocks, but negatively affected downstream fluid total pressure. Rao et al. investigated submerged and vane-type vortex generators[40]. The

authors observed that submerged showed better flow control potential, but geometry optimization was difficult due to spacing, length, and height sensitivities. Neumann et al. evaluated the affect of vortex generators on a S-shaped diffuser[41]. The authors demonstrated the ability to remove transitional separation through experimental pressure measurements. Further, Stumpf et al. examined exit distortion varying with time for the same S-shaped diffuser using vortex generators[42]. Although research has shown passive techniques have the ability to manipulate flow in a robust fashion, passive techniques do not have the ability to be manipulated during operation.

2.4.2. Active Flow Control

Active flow control techniques have the ability to be manipulated during operation. This provides more versatility and optimization for a wider range of operating conditions. McAuliffe et al. investigated the benefits steady jet blowing to suppress the boundary layer separation present on a turbine blade at low Reynolds number regimes[43]. A range of Reynolds numbers were tested and a required blowing ratio to significantly reduce profile loss was determined at each Reynolds number. This technique proved successful over the range tested, but a constant flow of air was required to suppress boundary layer separation. Seifert et al. investigated the effects of oscillatory air blowing to add momentum to the boundary layer with high-pressure compressed air[44]. The method demonstrated a delay in stall over the airfoil and a greater reduction in profile losses compared to steady blowing. The oscillatory blowing also reduced the total amount of momentum required to achieve the same performance compared to steady blowing due to the operation frequency not being constant. Vortex generator jets (VGJs) are another technique used for boundary layer separation control. VGJs inhibit separation by entraining added momentum into the lower velocity region near the surface. Volino et al. investigated the effects of oscillating vortex generator jets on the suction side of a low-pressure turbine (LPT) airfoil[31]. A cavity and plenum were created inside of a machined high-density foam airfoil to enable control of

the oscillating VGJs. Synthetic VGJs results showed the ability to control boundary layer separation on a LPT airfoil, and losses were substantially lower compared to a rectangular bar on surface to passively control flow.

Active flow control has also been researched in S-duct geometries. Different techniques have been implemented to improve the flow field and distortion present. Harper et al. evaluated the effectiveness of sucking and blowing on an offset S-duct inlet to manipulate flow[45]. Both methods produced similar results, and a combination of the two was determined to improve pressure recovery and decrease distortion the most significantly. Hamstra et al. performed an evaluation comparing microvanes and microjets in a short S-duct arrangement[46]. Results showed that microvanes were the better alternative compared to microjets, decreasing distortion by 5%. Gorton et al. evaluated the use of both passive and active flow control methods for a boundary layer ingesting inlet[47]. A passive vortex generator device and an active pneumatic pulsing actuator were compared, and results demonstrated that pulsing jets had the most significant impact on distortion, decreasing from 29% to 4.6%. The same inlet geometry had previously been investigated by Jenkins et al. using synthetic jets, but with no effective change due to flow control[48].

2.5. Plasma Flow Control Fundamentals

Plasma is described as a neutral substance containing free electrons and ionized atoms or molecules, exhibiting collective behavior either attractive or repulsive, based on Coulomb's Law[49]. Plasma is one of the four states of matter in the known universe and it can be produced by increasing the thermal energy of a substance until ionization occurs. A group of particles are classified a plasma if they meet a specific criteria. The criteria are macroscopic neutrality, Debye Shielding, and plasma frequency. Macroscopic neutrality refers to a condition when the net resulting electric charge for a plasma is zero. This takes place under equilibrium with no presence of external forces, sufficient plasma volume to contain a large amount of particles, and a small relative volume compared to characteristic

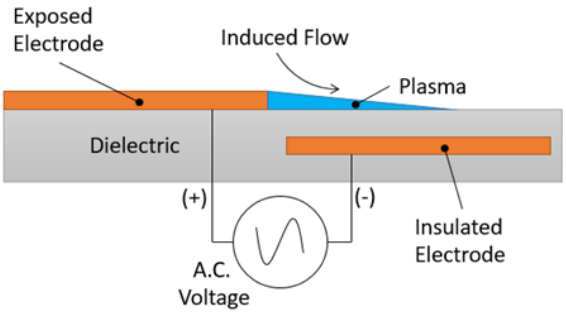

Figure 14: Surface-Dielectric-Barrier-Discharge (SDBD) Plasma Actuator.

lengths for density and temperature variation. Debye shielding may be discussed in terms of the characteristic length of plasma known as Debye length. This is the distance over which the influence of a electrically charged particle is influenced by surrounding particles inside the plasma. Plasma frequency is the stability of the plasma space charge neutrality[49]. Plasma has the ability to be disturbed from equilibrium, and return to a neutral state. The oscillations created have a corresponding frequency, which is the plasma frequency. With this understanding of plasma physics, flow control devices can be produced to take advantage of the unique characteristics produced due to plasma generation.

2.5.1. Plasma Actuators

Plasma actuators are a method of active flow control that has demonstrated potential in aerospace applications due to the induced flow that is generated at the surface. Figure 14 illustrates the setup of an asymmetric Surface-Dielectric-Barrier-Discharge (SDBD) plasma actuator. Asymmetric SDBD actuators take advantage of plasma being generated in a single direction as opposed to a symmetric SDBD actuator. Symmetric SDBD actuators consist of overlapping electrodes that produce plasma on both sides of the exposed electrode, reducing the magnitude of induced flow compared to an asymmetric arrangement producing concentrated plasma on one side. Plasma actuators have the capability to be optimized in terms of duty cycle, frequency, and power input. Plasma actuators manipulate the boundary layer by creating a body force in the boundary layer[50]. The actuator pro-

duces the force through the movement of free electrons during the air ionization process. When high voltage is passed through two electrodes separated by a dielectric barrier, a discharge occurs that ionizes the ambient air above the electrode surface and frees electrons. Once the electrons are free, the average direction of movement creates a body force at the surface. This induces higher velocity surrounding air and adds momentum, which accelerates the fluid in the boundary layer. The capability to alter flow properties make plasma actuators a viable method to apply to a wide range of flow control applications.

2.5.2. Plasma Flow Control Applications

Several different plasma actuators have been designed and evaluated previously. Examples include dielectric barrier discharge(DBD)[4], pulsed plasma jets[51–53], and localized arc filament plasma actuators(LAFPA)[33, 54, 55]. Corke et al. evaluated the use of steady plasma actuators on the suction surface of an airfoil for enhancing lift over a range of angles of attack[56]. Tests carried out in the low-speed wind tunnel at the U.S. Air Force Academy were measured with a lift-drag balance, and the actuators were designed to operate at a constant frequency, or steady. Results showed the plasma actuators produced changes in lift comparable to a mechanically actuated plane flap. Continuing from this previous application, Huang et al. experimentally investigated the use of an unsteady operating plasma actuator[57]. A turbine cascade of Pratt & Whitney Pak-B shaped blades was used to provide LPT operating conditions. Steady and unsteady plasma actuators were employed and effective in boundary layer separation control. The unsteady actuator was determined more effective when compared to the steady actuator, and did not require as much power to achieve the same effect. In addition, an optimal frequency was discovered for the unsteady plasma actuators that corresponded to the Strouhal number as a function of the LPT blade geometry. Previous work motivates current research of unsteady plasma to determine the effect of actuator frequency compared to steady operation to manipulate distortion in embedded ducts. Thomas et al. evaluated the use of unsteady plasma actuators

for flow control over a cylinder at varying duty cycles[58]. A plasma actuation frequency occurring at Strouhal number equal to 1 was found to be optimal;however, pulsing plasma at an associated frequency produced an additional tone. The additional tone was significant enough that continuous plasma operation was proposed for noise reduction. Additionally, total suppression of the boundary layer separation occurred at a duty cycle of 25 percent. Duty cycle is the percentage of time that the plasma actuator is operating relative to the operating frequency time interval. As duty cycle is reduced, power input to the plasma actuator necessary to manipulate boundary layer flow will be reduced.

CHAPTER III

EXPERIMENTAL STUDY

3.1. Experimental Setup

3.1.1. Facilities

Oklahoma State University Aerospace Propulsion and Power low-speed wind tunnel, shown in Figure 15, was used to conduct experiments for this study. It is an open-loop, draw-down wind tunnel that is powered by a 125 hp motor capable of freestream speeds up 95 ft/s. The test section has a 3-ft by 3-ft cross-sectional area and 8-ft length. Table 1 shows the instrumentation necessary to obtain desired test conditions and to characterize

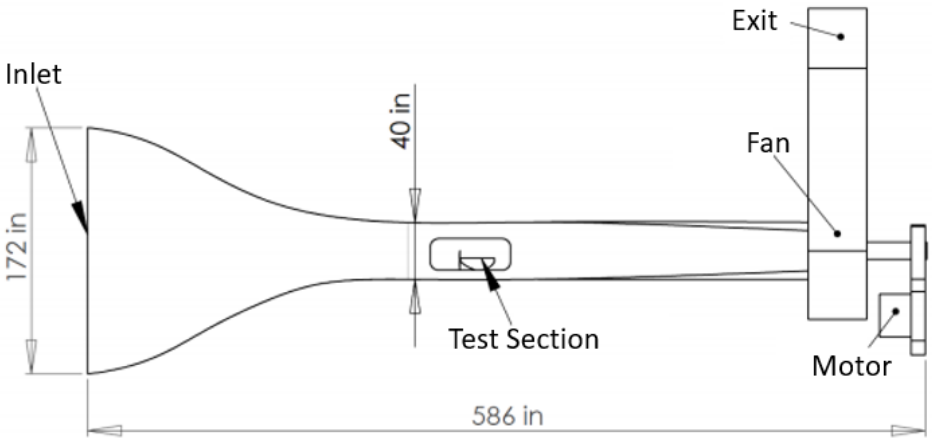

Figure 15: Oklahoma State University Low-Speed Wind Tunnel.

Table 1: Summary of Instrumentation

Instrument	Measured Value	Manufacturer	Range	Error
Pressure Transducer	q(ft/s)	Omega	0-2 in. H20	+/- 2% FS
Pressure Transducer	q(ft/s)	Omega	0-3 in. H20	+/- 2% FS
Hot Wire	U(ft/s)	Dantec Dynamics	1.64-1640 ft/s	+/- 2% FS
Thermocouple	T(F)	Extech Industries	32-122 F	+/- 0.1 F
Barometer	P(psi)	Extech Industries	0.145-15.95 psi	+/- 0.1 RO

performance. Pressure and temperature were measured with an Extech Industries Barometric Pressure, Humidity, Temperature data logger. A pitot-static probe and Omega pressure transducer were used to measure test section dynamic pressure inside the wind tunnel to calculate inlet freestream speed. A second pitot-static probe and Omega pressure transducer were used to measure test article dynamic pressure(q) at the exit of the embedded duct to calculate velocity. A Dantec Dynamics Constant Temperature Anemometer(CTA) hot-wire probe was used to measure velocity and velocity fluctuations at the test section inlet. Turbulence intensity was then calculated with the measured velocity fluctuations. A Dantec Dynamics automated, two-axis traverse was used to navigate the pitot-static probe precisely across the test section at the measurement plane. Path files were created in Excel and input in Labview to produce the desired measurement locations. Each location had a corresponding hold time of 6 seconds to allow for equilibrium to be reached. A National Instruments(NI) Data Acquisition system was used to collect data from pressure transducers, CTA, and thermocouple, which consisted of a NI 9220 analog-in card, a NI 9214 analog-out card, and a NI 9000 thermocouple card mounted in the NI cDAQ-9188 data acquisition base. A LabVIEW Virtual Instrument(VI) was developed to run the wind tunnel, operate the automated traverse, and read/write data for all testing presented in this paper.

Tests were conducted to characterize the flow in the wind tunnel test section and

provide information prior to installing the BLI rig. Values of interest included: boundary layer height at the test section inlet and inlet turbulence intensity. A pitot-static and single-axis hot wire probe were used to determine test section inlet boundary layer height. First, a pitot-static probe was manually traversed to record average velocities at larger incremental steps of 1, 2, and 3 inches from the tunnel wall. With no change in velocity compared to the freestream, the hot wire probe was traversed from 0.5 to 1 inch from the tunnel wall. This produced a boundary layer height of 0.7 inches. Inlet turbulence intensity(TI) was also determined using a single-axis hot wire probe. Turbulence intensity is defined as

$$\mathrm{TI} \equiv \frac{u'}{U} \tag{8}$$

where u' is standard deviation of turbulent velocity fluctuations and U is the average velocity. Measurements were taken a sufficient distance outside of the boundary layer and over a range of freestream tunnel speeds from 62 to 91 ft/s. Turbulence intensity was observed ranging from 1.15 to 1.40 %.

3.1.2. BLI Rig

A notional boundary layer ingestion rig was designed to produce a representative distorted flow field, which is shown in Figure 16. The BLI rig consisted of an inlet duct

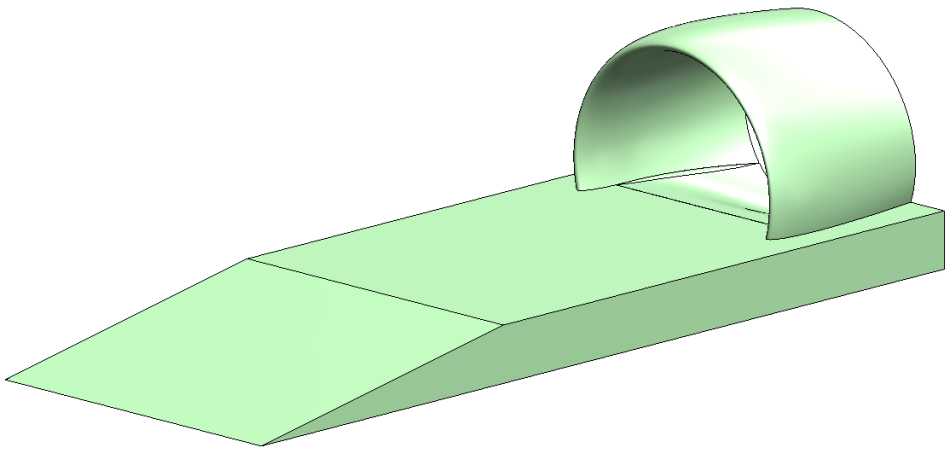

Figure 16: Initial Boundary Layer Ingestion Rig in Solidworks.

and ramp assembly to produce a distorted flow at the measurement plane location. Duct geometry was developed with consideration of being employed on a slow flying, less than Mach 0.3, unmanned aircraft platform.

3.1.3. Contracting and Diffusing Inlets

Two geometry types may be used when designing an embedded engine inlet, contracting or diffusing. The geometry selected is dependent on the specific aircraft and flight condition being experienced by the inlet. Commercial transport aircraft typically operate at speeds greater than a the fan and compressor are designed to experience. For this reason, a diffuser is needed upstream to reduce the incoming air speed to the intended design value of Mach 0.6 [59]. When flights speeds lower than Mach 0.6 are experienced, a contracting inlet may be employed to increase the freestream velocity upstream of the fan or compressor face. This study will employee a contracting inlet duct geometry based on representative flight speeds not exceeding Mach 0.3.

Results of this study will attempt to determine effectiveness of plasma actuators to manipulate distortion present in a contracting duct geometry. Flow properties may differ from contracting to diffusing type inlet ducts. One example would be the development of vortices around the connection of the ramp surface to the duct lip. The intensity of these vortices, or horseshoe vortices as commonly referred, may change due to the accelerating nature of contracting geometry, as opposed to decelerating through diffusion. A study to determine effects present in a diffusing duct would be needed to definitively state plasma flow control effectiveness for embedded engine inlets in general.

3.1.4. Duct and Ramp Design

The inlet BLI ramp has a 17-inch, 10° slope to a 23-inch horizontal section before transitioning down to a 2-inch offset, 10-inch diameter circular exit. The transition from horizontal surface to offset circular exit is achieved with 10 section planes evenly spaced 1

inch apart with a unique sketch contouring to the duct geometry on each plane. A lofted cut was produced with the sketches, and guide curves were used to smooth wall interactions. The bottom dead center location of the duct exit was 1-inch from the floor of the wind tunnel test section. This was chosen to ensure adequate material to reduce the potential for cracking. The overall entry inlet ramp was 48 inches long and had a blockage area of $54in^2$. The inlet duct has a 10-inch axial length and a 1.25:1 area contraction ratio. A standard NACA 0012 airfoil was obtained from Airfoil Tools' web page and modified to obtain the desired 10-inch circular exit geometry.

The BLI rig was produced by a computer numerically controlled(CNC) router from high-density foam. The CNC router is a. Multiple pieces were produced from a single sheet of high-density foam due to operating depth of the router bed, which was 3 inches. Figure 17 illustrates the inlet duct pieces produced. The duct pieces were connected together with Loctite quick-set epoxy rated to 3200 psi. Another limitation was the ability to cut variable geometries both inside and outside duct surfaces. Figure 17 shows the interior wall geometry that was maintained while the exterior was cut with guide steps, but unable to be fully tapered. The inlet and exit duct foam was RenShape 5014 Polyurethane Foam Board and the inlet and exit ramp foam was Renshape 5025. RenShape 5014 is a light-density foam recommended for lightweight appearance models and was readily in stock. Although the foam was very lightweight, it took almost three times as long to prepare. 3M Sandblaster Pro 220, 400, 800, and 1500 grit sand paper was used to achieve adequate surface finish. Figure **??** depicts the inlet duct post-sanding before primer and sealant were applied. This process was common for all components fabricated out of foam. The inlet and exit ramps were made from RenShape 5025, which is a medium-density foam recommended for improved workability and surface finish compared to RenShape 5014. The preparation time was substantially reduced, partly due to the less complex geometry of the ramp, but mostly due to the 5025 foam workability. The final task was to secure the inlet duct and ramp in a way that was not permanent, but strong enough to withstand vibration

Figure 17: Duct after CNC production illustrating geometry of exterior (left), duct after CNC production illustrating internal geometry (center), duct after epoxy and sanding process (right).

during wind tunnel testing. Holes were drilled in the inlet duct and threaded collars were epoxied inside to provide a mounting structure. Counter-sunk holes were then drilled in the inlet ramp to allow threaded bolts to pass through the ramp bottom in order to provide a secure connection to the duct. With the assembly complete, initial wind tunnel tests were conducted to evaluate initial velocity profiles at the embedded duct exit plane.

The initial inlet duct and ramp were tested in the wind tunnel to evaluate velocity profiles measured at the duct exit plane. Tests were conducted at 3 velocities with corresponding voltage inputs to the wind tunnel variable frequency drive(VFD). These voltages

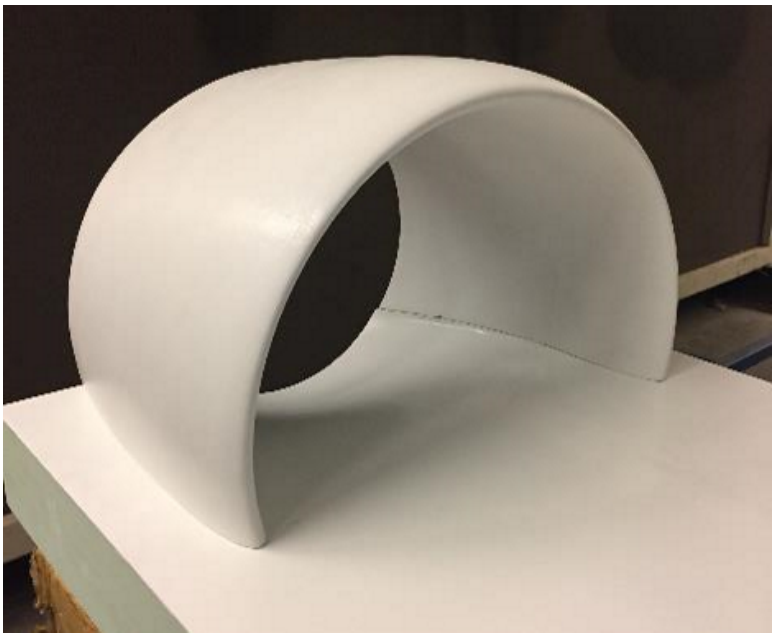

Figure 18: Inlet Duct and Ramp final connections.

were 7, 8, and 9 Volts and corresponding velocities are 63, 72, 81 ft/s. A pitot-static probe traversed the duct exit plane using circular measurement paths created in Excel and input to the LabVIEW VI. Initial data was difficult to draw conclusions from and only moderately resembled a typically boundary layer profile. Five more tests were performed before flow visualization was conducted in the wind tunnel to provide qualitative insight. Three 20,000 ft^3/min smoke machines were set up to provide the seeding. Recirculation was assumed to be occurring at multiple locations downstream of the BLI rig, which would cause pitot-static data to be flawed during initial tests.

A second iteration to the design was necessary to achieve adequate exit duct length. An exit duct, ramp and side ramps were developed to reduce recirculation and effectively transition the flow away from the measurement location. The exit duct overall length was 8 inches and geometry matched the circular inlet exit 10-inch diameter. The exit duct mated up to an exit ramp that formed a 10-inch cylindrical diameter maintaining constant area from the measurement plane to the end of the duct. The exit ramp was 32-inches long and had an 8° transition angle to the floor of the wind tunnel test section. A unique feature of the exit ramp is the 1-inch traverse slot that was cut with a CNC router to allow a pitot-static probe to measure inside of the duct. Both components were manufactured out of medium-density foam using similar techniques described previously. Side ramps were incorporated into the final design to further improve the flow field and reduce effects due to recirculation or wind tunnel wall/ramp interactions. Figure 19 illustrates the 4 ramps that were manufactured to border the BLI rig. Each of the four ramps were manufactured using

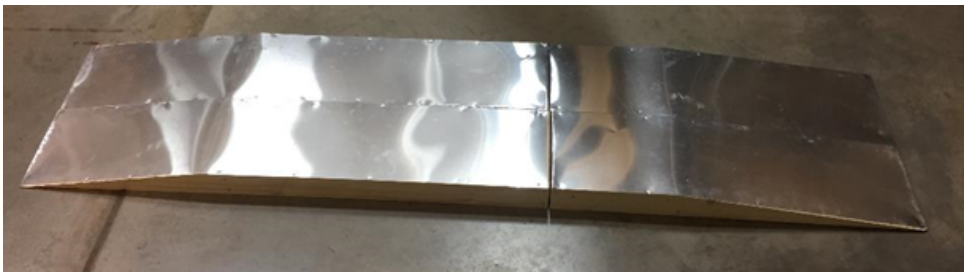

Figure 19: Front and rear side ramps to reduce recirculation and wall effects.

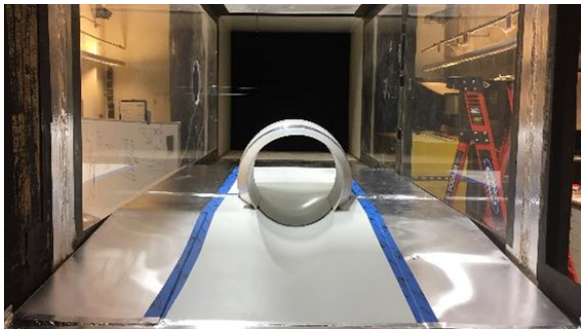

Figure 20: Picture displaying the final BLI rig assembled and mounted in the OSU wind tunnel test section.

1"x4" lumber purchased at Lowe's. Wood frames were constructed with the necessary entrance and exit angles, and covered using 1/16" thick aluminum sheet metal to obtain the desired surface finish. Figure 20 shows the final design assembled and mounted in the wind tunnel. Tests were conducted over a range of wind tunnel velocities, 60 to 90 ft/s, and measurements were taken at the duct exit plane.

3.1.5. Plasma Actuator

A surface-dielectric-barrier-discharge (SDBD) plasma actuator was evaluated to manipulate flow through an embedded duct. Figure 21 displays the different components that make up the plasma actuator in this study and the component locations. The dielectric material used is electrical-insulating mica sheet 0.024 inches thick. Mica was chosen for high dielectric strength at 635 V/mil and resistance to etching that may occur over prolonged use. Actuator electrodes are highly conductive copper electrical tape with conductive adhesive 0.25 inches wide and 0.0035 inches thick. SDBD actuators commonly use an insulating material to encapsulate the electrode on the bottom surface to prevent an electric short from one electrode to the other. 3M high voltage electrical tape 0.75 inches wide and rated to 69,000 V was used for insulating. Wire connections to electrodes were insulated with standard black electrical tape.

Figure 22 shows a completed SDBD after assembly. The mica sheet was scored

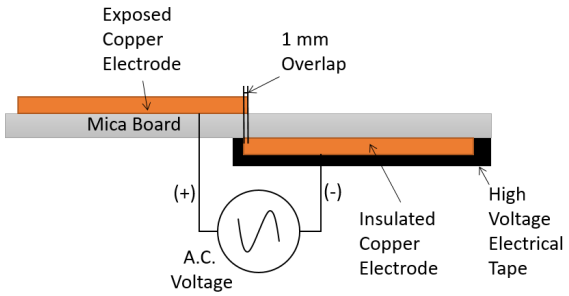

Figure 21: Surface-dielectric-barrier-discharge plasma actuator component layout.

with a razor knife and broken at the scored location, and sheet edges were sanded with 800 grit sandpaper. The electrode geometry commonly used is asymmetric with small (1 mm) overlap with the surface electrode upstream of the encapsulated electrode. Three configurations of actuator locations were tested for this study. Figure 23 details the configurations and corresponding locations relative to the inlet duct lip. Actuators for Configuration 1 and 2 were both 11 inches in length and 1 inch wide. This length was chosen to provide the largest influence while still fitting inside of the inlet duct structure. Two lengths of plasma actuators were manufactured due to the geometry of the BLI ramp. The actuator for Configuration 3 was 5.5 inches in length due to the desire to mount on the horizontal surface of the ramp. Also, Configuration 3 was mounted on the ramp transitional portion and had a relative angle of 15 degrees compared to Configurations 1 and 2.

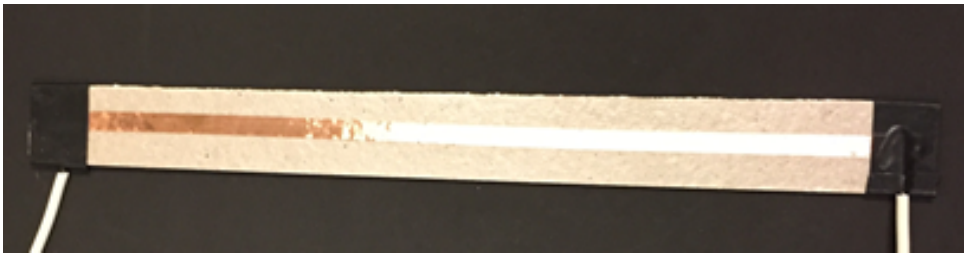

Figure 22: Top view of assembled plasma actuator.

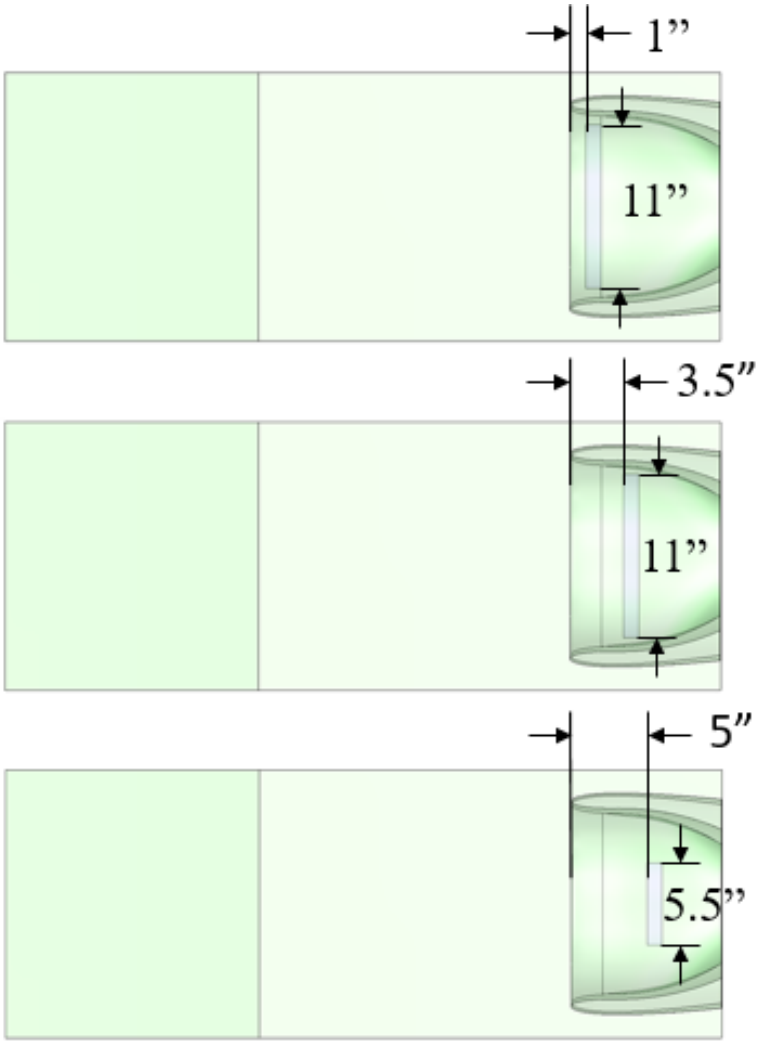

Figure 23: Plasma configurations evaluated in this study: Configuration 1 (Top) - 1 inch aft duct inlet, Configuration 2 (Middle) - 3.5 inches aft duct inlet, Configuration 3 (Bottom) - 5 inches aft duct inlet.

3.1.6. Test Matrix

Tests performed in this study are shown in Table 2. Wind tunnel velocities were evaluated from 63 to 81 ft/s, and velocities below 63 ft/s were considered meaningless for representative flight speeds. Multiple frequencies were tested to evaluate the effect of frequency on distortion intensity. Assuming Strouhal number of 0.2 and characteristic length of 10 inches, frequency content can be estimated. Plasma actuator frequency may

be selected to match the content frequency or increased to observe the effect of higher frequency pulsing. Pulsing at a higher frequency than content frequency is expected to be more effective. Shedding frequency was also considered when selecting pulsing frequency. The frequency a vortex sheds can be determined using the distance from the entrance lip of the inlet to the measurement plane and the wind tunnel freestream velocity. For example, a duct length of 12 inches with a freestream velocity of 60 ft/s would take 0.0167 seconds, correlating to a frequency of 166 Hz. Frequencies evaluated were 0 Hz or continuous operation, and 10, 100, and 166 Hz.

Table 2: Experimental Test Matrix

Configuration	Wind Tunnel Speed	Plasma Operation	Frequency
1	63-82 ft/s	On-Off	0,10,100,166 Hz
2	63-82 ft/s	On-Off	0,10,100,166 Hz
3	63-82 ft/s	On-Off	0,10,100,166 Hz

CHAPTER IV

RESULTS

Dynamic pressure measurements were obtained to observe the effects of plasma flow control on distortion in a BLI arrangement. Measurements were taken at designated points on a circular profile that was created using polar coordinates. Numerous profiles were tested to reduce number of measurement points while maintaining a sufficient resolution to determine affect on distortion. Figure 24 illustrates the path generated and implemented to obtain measurements for this study. Maximum and minimum actuator configurations will be discussed, Configuration 1 at 1 inch aft and Configuration 3 at 5 inches aft of duct inlet. Configuration 2 will not be discussed due to the similarities in results compared to Configuration 1.

4.1. BLI Arrangement Characterization

Experiments were performed to evaluate distortion intensity and qualitatively assess cross-sectional velocity profiles for a notional BLI arrangement without plasma actuators installed. Figure 25 illustrates a 3-dimensional velocity profile at the BLI arrangement measurement plane for freestream velocity of 63 ft/s. The x and y axes represent the normalized location of the pitot-static probe inside of the wind tunnel test section. The center of the BLI arrangement corresponded to an x and y location of 0 and 0 inches. The z

axis, which goes into the page, represents normalized velocity measured inside of the BLI arrangement. Velocities were normalized by the duct centerline velocity. Dynamic pressure measurements were used to calculate distortion intensities, which produced a dynamic circumferential distortion intensity of 1.02% and a radial distortion intensity of 0.008%. Consistent with previous work, circumferential distortion intensity is the main contribution to distortion for the embedded duct. Radial distortion will be reported on all figures, but will not be discussed further due to the negligible contribution.

The velocity profile for the lower portion of the BLI arrangement can be further evaluated with Figure 26. The figure illustrates the lateral view of the same 3-dimensional velocity profile shown previously for freestream velocity of 63 ft/s. The x axis depicts the normalized location axially inside the duct, but the normalized velocity is depicted on the y axis to better represent the magnitude and radial locations. The radial locations are shown as contour lines and the height of the contour line indicates the velocity magnitude at each lateral location, indicated on the x-axis. The magnitude of the bottom dead center measurement can clearly be observed below 85% of the duct centerline freestream velocity. Symmetry of the profile can also be observed with this representation.

4.1.1. Freestream Velocity Effect

Tests were performed to evaluate the effect of freestream velocity on the BLI distortion intensity and velocity profiles. Figure 27 shows a 3-dimensional velocity profile at the BLI arrangement measurement plane for freestream velocity of 72 ft/s. Comparing Figures 25 and 27, an increase in circumferential distortion intensity of 12% is observed. Figure 29 shows a 3-dimensional velocity profile at the BLI arrangement measurement plane for freestream velocity of 81 ft/s. Comparing Figures 27 and 29, an increase in circumferential distortion intensity of 31% is observed. A trend is observed with increasing freestream velocity such that distortion intensity appears to increase with increasing wind tunnel velocity. This agrees with results provided by previous research, which demonstrated increasing free

stream velocity reducing pressure recovery capability [60]. Skin friction was the primary function for total pressure loss at lower flight speeds; however, as flight speeds increased, duct geometry and BLI effects were the majority of losses. This is noteworthy integrating BLI propulsion systems onto unmanned aircraft that operate at lower flight speeds.

Comparing Figures 26, 28, and 30, the magnitude of the radial locations is better observed. The radial locations are shown as contour lines and the height of the contour line indicates the velocity magnitude at each lateral location, indicated on the x-axis. The magnitude of bottom dead center measurements appears to stay relatively similar between 0.82 and 0.84 %, but the shape of the profile changes significantly along the x axis. The profile widens and distortion area of the contour lines appears to be increasing, which could be caused by the BLI effects producing a more turbulent boundary layer as the wind tunnel freestream increases.

A plot was produced using the vertical centerline measurements to compare multiple conditions corresponding to the relative freestream velocity. Figure 31 shows the differences in velocity profiles as wind tunnel velocity is increased. As freestream velocity is increased, the normalized velocity values within the boundary layer begin to shift left or go down in magnitude. The observed velocity profile behavior agrees with the increase in distortion intensity as wind tunnel velocity is increased. Knowing the behavior of the BLI arrangement prior to installing plasma actuators allows for a more thorough understanding of the flow characteristics due to geometry.

4.2. Plasma Actuator Effect

4.2.1. Installed Actuator

An evaluation of the effect of attaching a plasma actuator to the surface of a BLI experimental arrangement was also performed. For this study, plasma actuators were not embedded in the ramp, consequently creating a boundary layer trip. The results in this

section will become the new baseline to determine the effectiveness of plasma actuators for manipulating distortion through the embedded duct arrangement. Results in this section will be presented for a constant wind tunnel velocity of 63 ft/s for comparison purposes. Figure 32 shows a 3-dimensional velocity profile for an installed actuator, with no plasma generation, at Configuration 1, and freestream velocity of 63 ft/s. Circumferential distortion intensity of 1.26% was observed, which is 19% higher than the baseline case with no actuator installed. 34 shows a 3-dimensional velocity profile for an installed actuator, no plasma generation, Configuration 3, and freestream velocity of 63 ft/s. Circumferential distortion intensity of 1.26% was observed, which is 19% higher than the baseline case with no actuator installed.

Comparing Figures 26, 33 and 35 the magnitude of the radial locations is better observed. The radial locations are shown as contour lines and the height of the contour line indicates the velocity magnitude at each lateral location, indicated on the x-axis. The magnitude of bottom dead center measurements changes significantly with the addition of plasma actuators, but the shape of the profile remains relatively constant along the x axis. The actuator for Configuration 1 has the lowest normalized velocity magnitude compared to the baseline and Configuration 3, which suggests actuator location impacts the velocity magnitude.

A plot was produced using the vertical centerline measurements to compare multiple conditions corresponding to the relative freestream velocity and actuator locations. Figure 36 shows the differences in velocity profile as actuator location is varied while at a wind tunnel velocity of 63 ft/s. Configuration 1 and 3 have similar circumferential distortion intensity, but do not have equal normalized velocities at the bottom measurement location in the BLI duct. The increase in distortion intensity due to addition of plasma actuators and dissimilar velocity profiles for both configurations confirms the need to update the baseline case moving forward.

4.2.2. Effect of Steady Plasma Actuator

An evaluation of the effect of steady plasma generation was conducted. Plasma was generated uniformly at 9 kV for all experiments. Figure 37 shows a 3-dimensional velocity profile for an installed actuator, generating plasma continuously, at Configuration 1, and freestream velocity of 63 ft/s. Comparing Figures 32 and 37, an increase in circumferential distortion intensity of 2% is observed. Increasing distortion intensity with the operation of steady plasma is an unexpected result and may be due to the operating condition enhancing the distortion inherently present in the BLI arrangement. Figure 39 shows a 3-dimensional velocity profile for an installed actuator, generating plasma continuously, at Configuration 3, and freestream velocity of 63 ft/s. Comparing figs. 34 and 39, an increase in circumferential distortion intensity of 6% is observed. Similarly to the previous result for Configuration 1, distortion intensity increased with the operation of steady plasma.

Comparing Figures 33 to 38 and 35 to 40, the magnitude of the radial locations is better observed. The radial locations are shown as contour lines and the height of the contour line indicates the velocity magnitude at each lateral location, indicated on the x-axis. The normalized velocity magnitudes are lower for both Configuration 1 and 3 with the addition of steady plasma, but the shape of the profiles remains relatively constant along the x axis. Although the velocity magnitudes were reduced when steady plasma was generated, a conclusion is unable to be made in regards to the cause.

A plot was produced using the vertical centerline measurements to compare multiple conditions corresponding to the relative freestream velocity and actuator locations. Figure 44 shows the effect of a plasma actuator operating continuously for both Configurations 1 and 3 at a wind tunnel velocity of 63 ft/s compared to relative baseline cases. Both configurations experience a reduction in normalized velocities at the bottom measurement location in the BLI duct when compared to relative baseline cases. The steady plasma results do not provide clear information to make conclusions and further testing is required to evaluate any benefits.

4.2.3. Effect of Pulsed Plasma Actuator

An evaluation of the effect of pulsing a plasma actuator at different locations was conducted. Plasma was generated uniformly at 9 kV for all experiments. The 10 Hz operating condition will be discussed here as all other frequencies demonstrated insignificant results. Figure 42 shows a 3-dimensional velocity profile for a plasma actuator operating at 10 Hz, in Configuration 1, and at 63 ft/s freestream velocity. Comparing Figures 32 and 42, an increase in circumferential distortion intensity of 3% is observed. Increasing distortion intensity with the operation of pulsed plasma is an unexpected result and may be caused by a number of reasons. Actuator location and in-phase frequency are two factors that may be enhancing the distortion inherently present in the BLI arrangement. Figure 49 shows a 3-dimensional velocity profile for a plasma actuator operating at 10 Hz, in Configuration 3, and at 63 ft/s freestream velocity. Comparing Figures 34 and 49, a decrease in circumferential distortion intensity of almost 9% is observed, which appeared to have an influence on the distortion intensity magnitude more than any other condition.

Comparing Figures 33 to 43 and 35 to 50, the magnitude of the radial locations is better observed. The radial locations are shown as contour lines and the height of the contour line indicates the velocity magnitude at each lateral location, indicated on the x-axis. The normalized velocity magnitude for Configuration 1 is lower than Configuration 3 with the addition of pulsed plasma at 10 Hz, but the shape of the profiles remains relatively constant along the x axis. Although the velocity magnitudes were reduced when steady plasma was generated, a conclusion is unable to be made in regards to the cause.

A plot was produced using the vertical centerline measurements to compare multiple conditions corresponding to the relative freestream velocity and actuator locations. Figure 44 shows the effect of a plasma actuator operating continuously for both Configurations 1 and 3 at a wind tunnel velocity of 63 ft/s compared to relative baseline cases. Both configurations experience a reduction in normalized velocities at the bottom measurement location in the BLI duct when compared to relative baseline cases. The steady plasma re-

sults do not provide clear information to make conclusions and further testing is required to evaluate any benefits.

4.3. Summary of Experimental Results

An evaluation of distortion intensity and a qualitatively assessment of cross-sectional velocity profiles for a notional BLI arrangement with and without plasma actuators was conducted. Velocities were normalized by the duct centerline velocity. Dynamic pressure measurements were used to calculate distortion intensities. Table IV. provides a summary of distortion intensities observed across all testing conditions. Distortion increased with the addition of plasma actuators to the surface of the BLI arrangement, which was expected. Based on this increase, a new baseline was necessary to measure the effectiveness of plasma actuators operating at steady and unsteady conditions. Steady plasma operation showed no ability to reduce distortion intensity present, increasing the magnitudes for both Configuration 1 and 3. Multiple pulsed plasma actuator frequencies were evaluated to determine a corresponding effect on distortion intensity. Pulsing plasma at 100 and 166 Hz did not show a significant change in distortion intensity, increasing the magnitude for most cases. Pulsing plasma at 10 Hz for Configuration 1 did not show a significant change in distortion intensity; however, at Configuration 3 the distortion intensity decreased by almost 9%. The reduction in distortion intensity at 10 Hz was the largest change witnessed for the conditions tested.

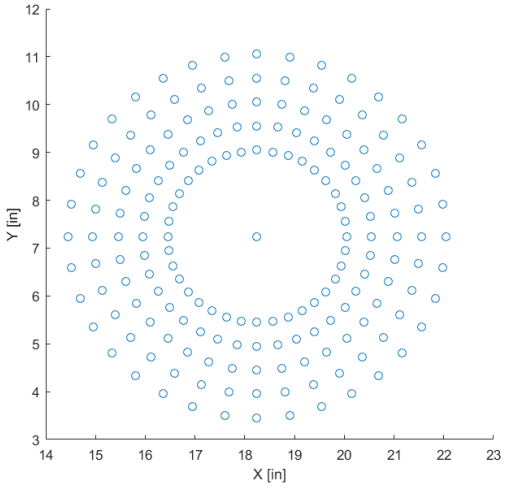

Figure 24: Automated traverse path created to obtain measurements inside BLI arrangement.

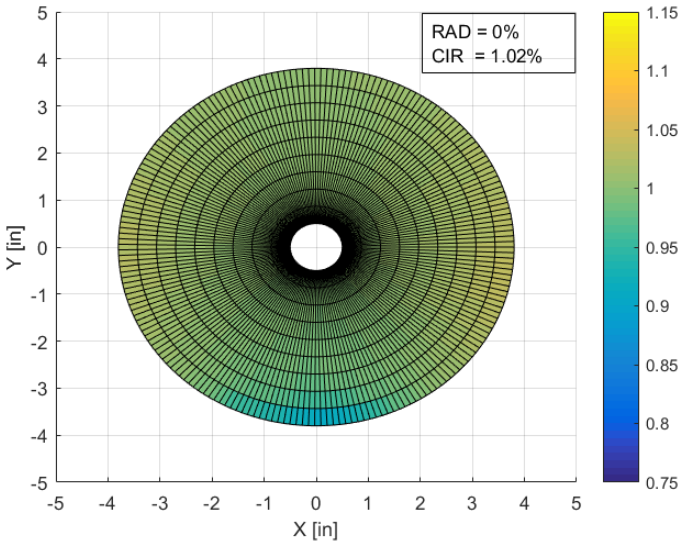

Figure 25: Velocity profile for no plasma actuators and freestream velocity of 63 ft/s condition.

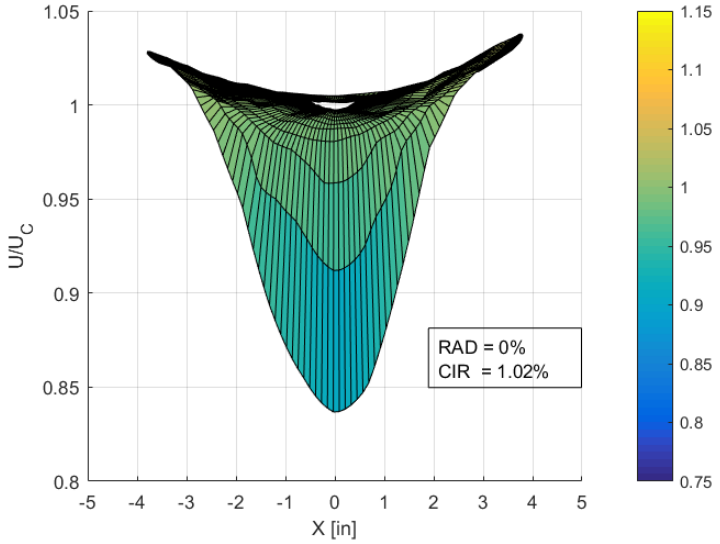

Figure 26: Lateral view of velocity contours for no plasma actuators and freestream velocity of 63 ft/s conditions.

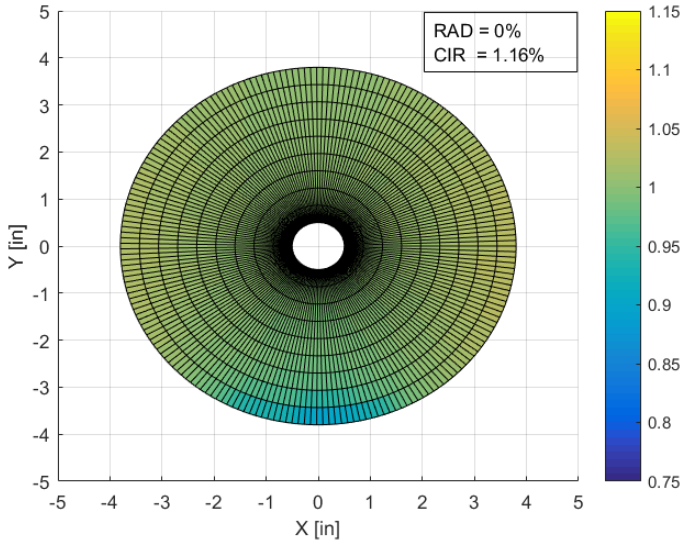

Figure 27: Velocity profile for no plasma actuators and freestream velocity of 72 ft/s condition.

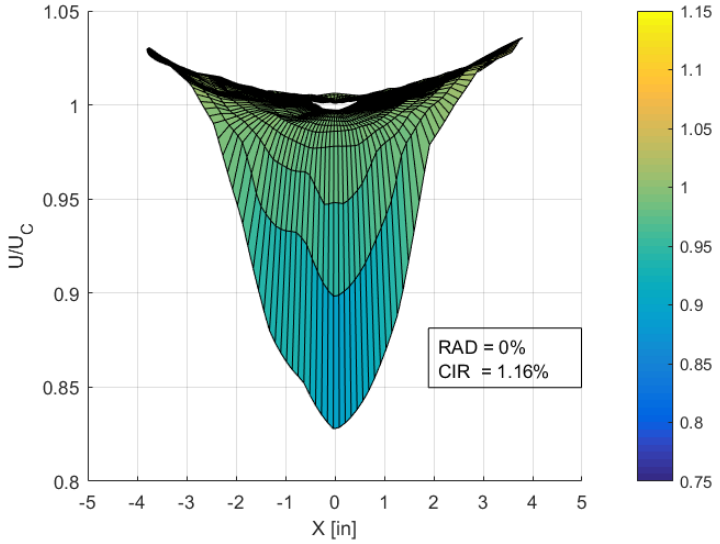

Figure 28: Lateral view of velocity contours for no plasma actuators and freestream velocity of 72 ft/s conditions.

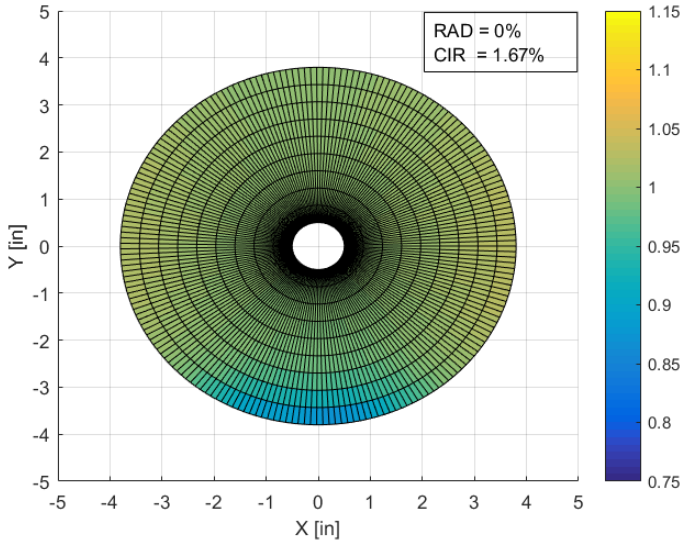

Figure 29: Velocity profile for no plasma actuators and freestream velocity of 81 ft/s condition.

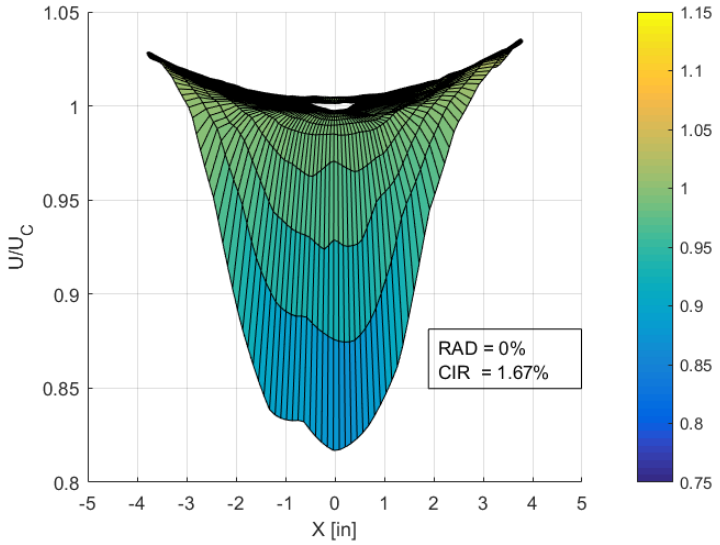

Figure 30: Lateral view of velocity contours for no plasma actuators and freestream velocity of 81 ft/s conditions.

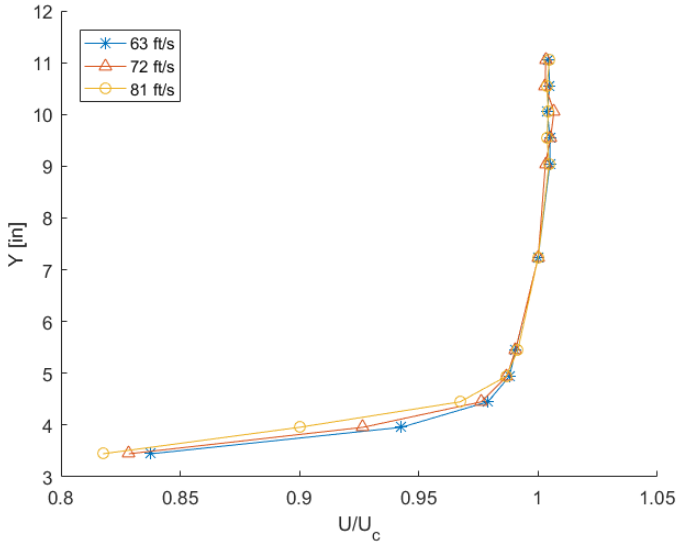

Figure 31: Velocity profile demonstrating the effect of increasing freestream velocity.

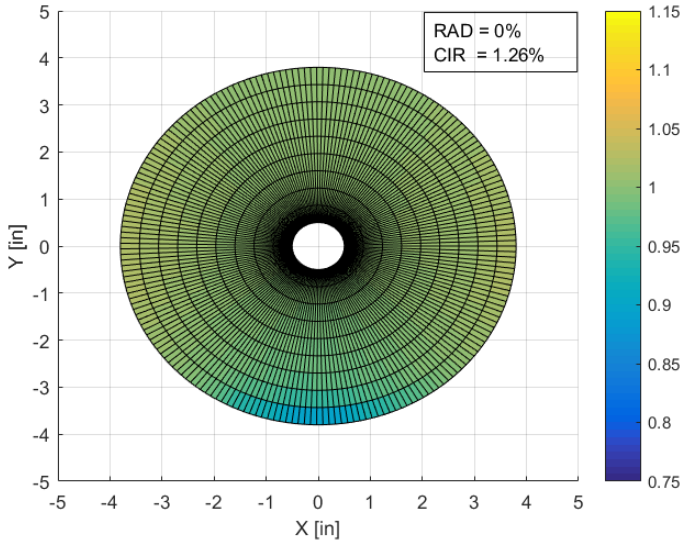

Figure 32: Velocity profile for installed plasma actuator at Configuration 1 and freestream velocity of 63 ft/s condition.

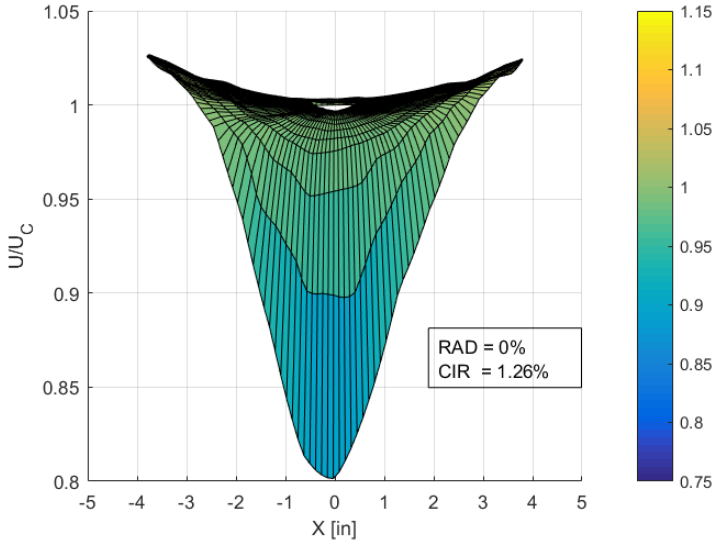

Figure 33: Lateral view of velocity contours for installed plasma actuator at Configuration 1 and freestream velocity of 63 ft/s conditions.

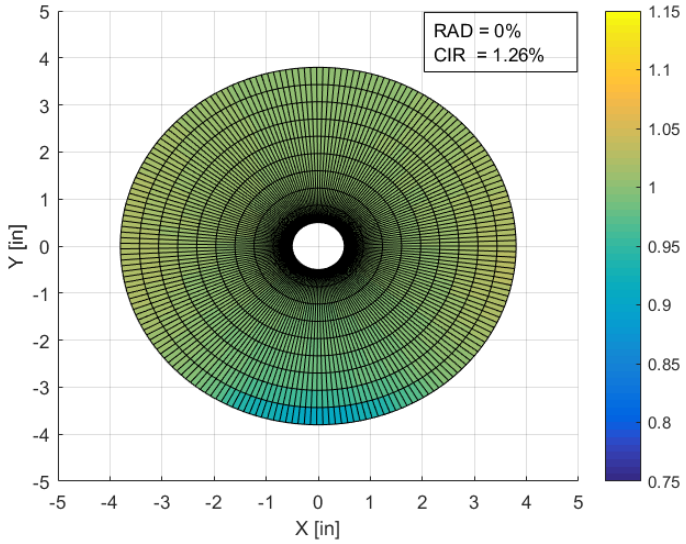

Figure 34: Velocity profile for installed plasma actuator at Configuration 3 and freestream velocity of 63 ft/s condition.

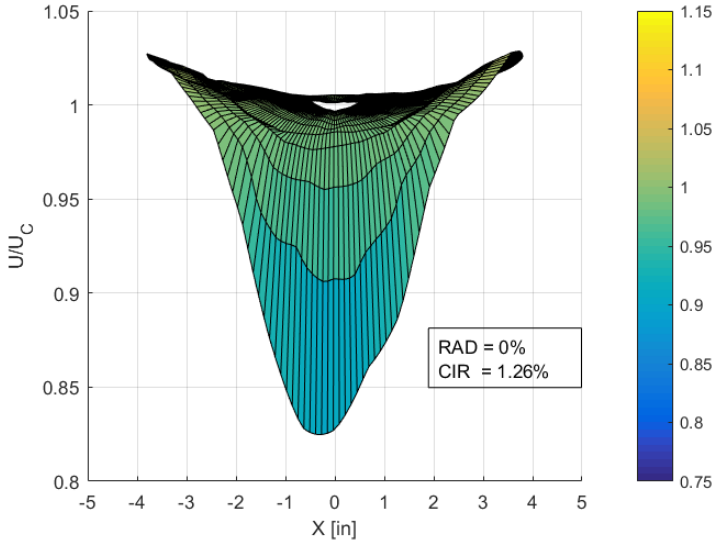

Figure 35: Lateral view of velocity contours for installed plasma actuator at Configuration 3 and freestream velocity of 63 ft/s conditions.

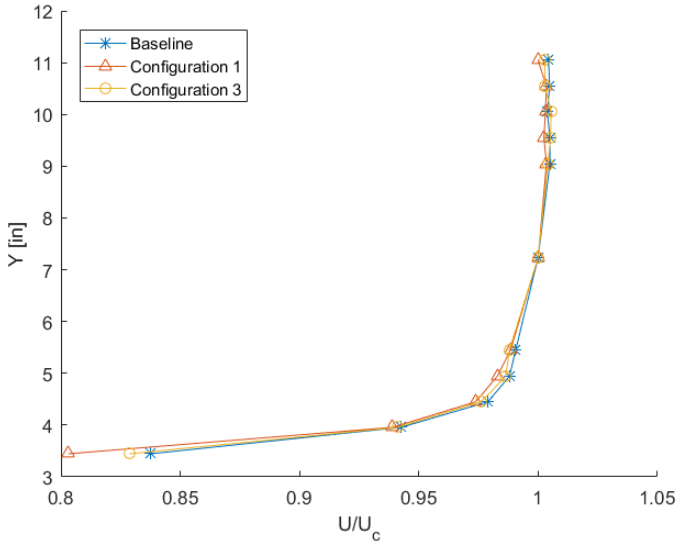

Figure 36: Velocity profile demonstrating the effect plasma actuator installation at different configurations for 63 ft/s.

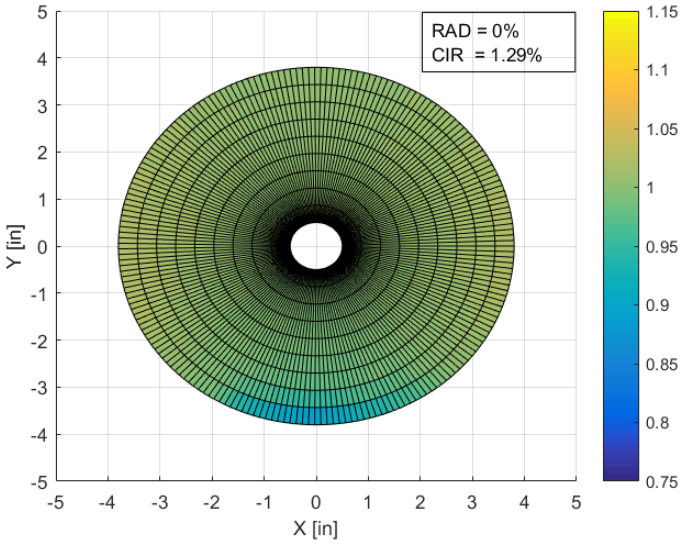

Figure 37: Velocity profile for plasma actuator operating continuously at Configuration 1 and freestream velocity of 63 ft/s condition.

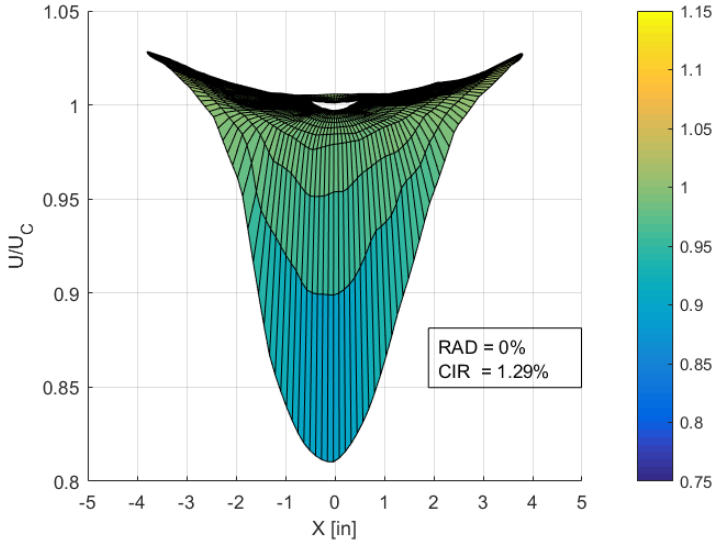

Figure 38: Lateral view of velocity contours for plasma actuator operating continuously at Configuration 1 and freestream velocity of 63 ft/s conditions.

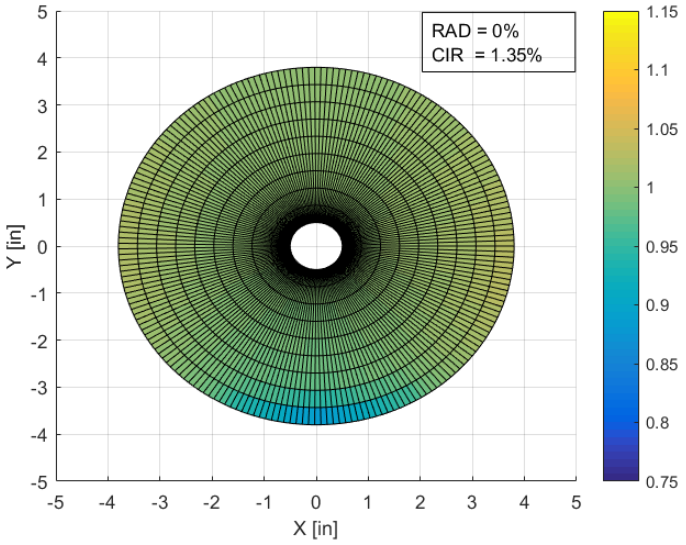

Figure 39: Velocity profile for plasma actuator operating continuously at Configuration 3 and freestream velocity of 63 ft/s condition.

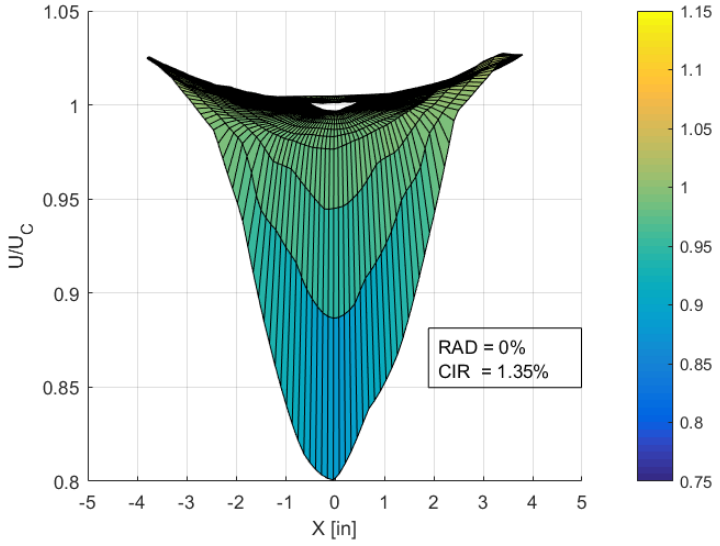

Figure 40: Lateral view of velocity contours for plasma actuator operating continuously at Configuration 3 and freestream velocity of 63 ft/s conditions.

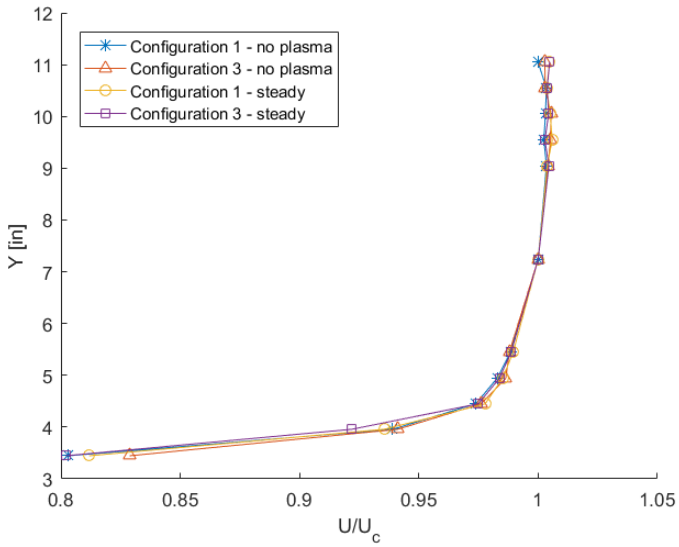

Figure 41: Velocity profile demonstrating the effect of a plasma actuator operating continuously at different configurations for 63 ft/s.

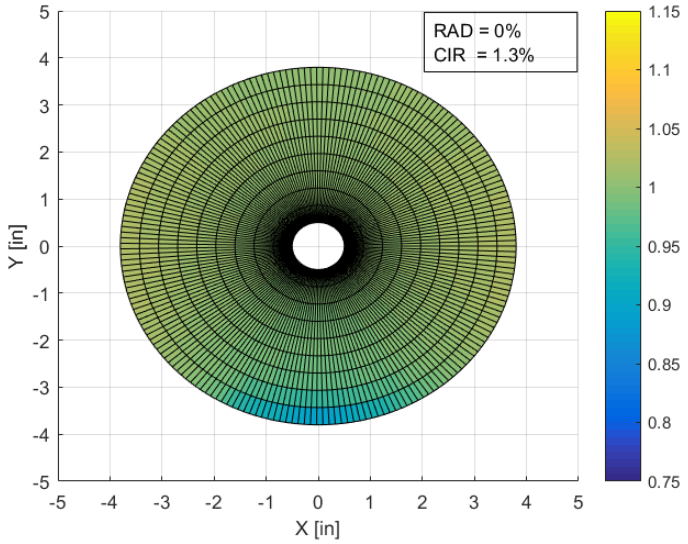

Figure 42: Velocity profile for a 10 Hz pulsed plasma actuator at Configuration 1 and freestream velocity of 63 ft/s condition.

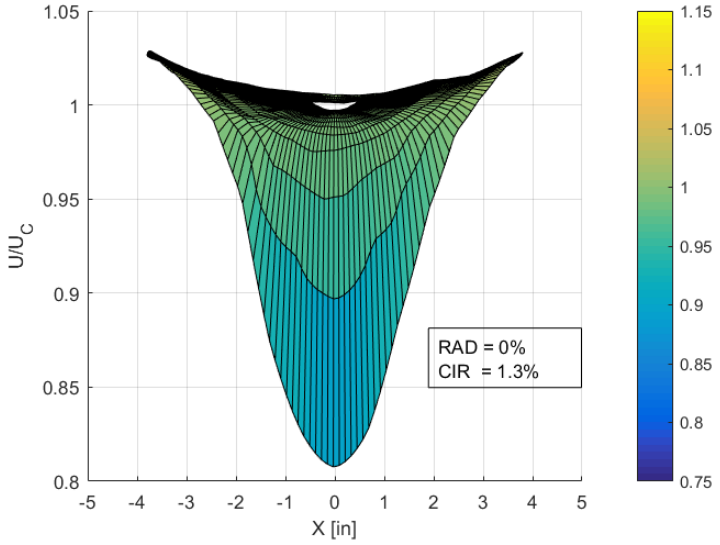

Figure 43: Lateral view of velocity contours for a 10 Hz pulsed plasma actuator at Configuration 1 and freestream velocity of 63 ft/s conditions.

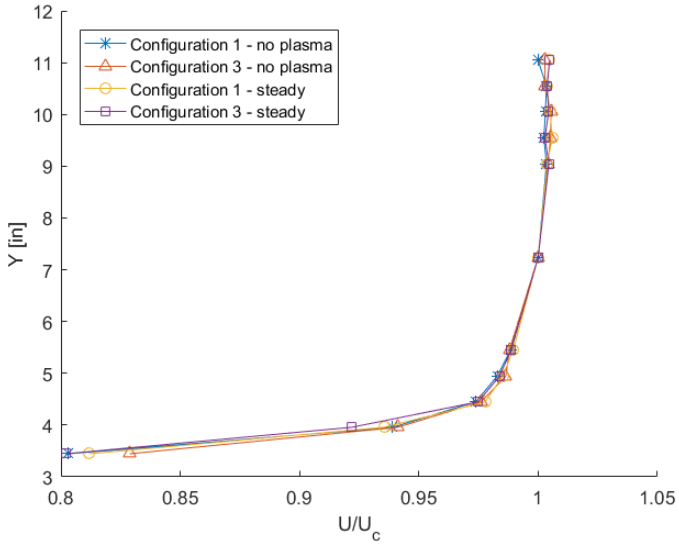

Figure 44: Velocity profile demonstrating the effect of a 10 Hz pulsed plasma actuator at different configurations for 63 ft/s.

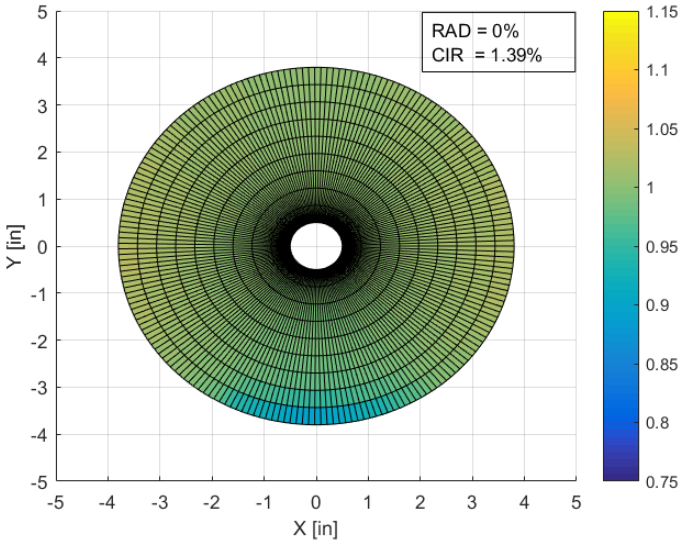

Figure 45: Velocity profile for a 100 Hz pulsed plasma actuator at Configuration 1 and freestream velocity of 63 ft/s condition.

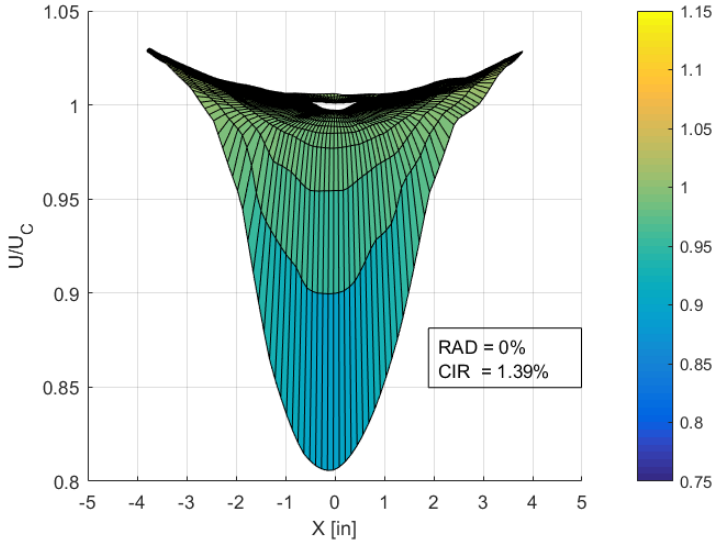

Figure 46: Lateral view of velocity contours for a 100 Hz pulsed plasma actuator at Configuration 1 and freestream velocity of 63 ft/s conditions.

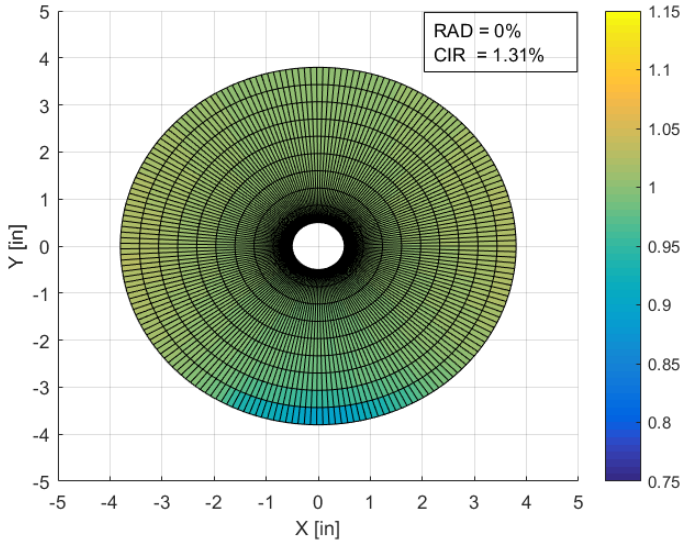

Figure 47: Velocity profile for a 166 Hz pulsed plasma actuator at Configuration 1 and freestream velocity of 63 ft/s condition.

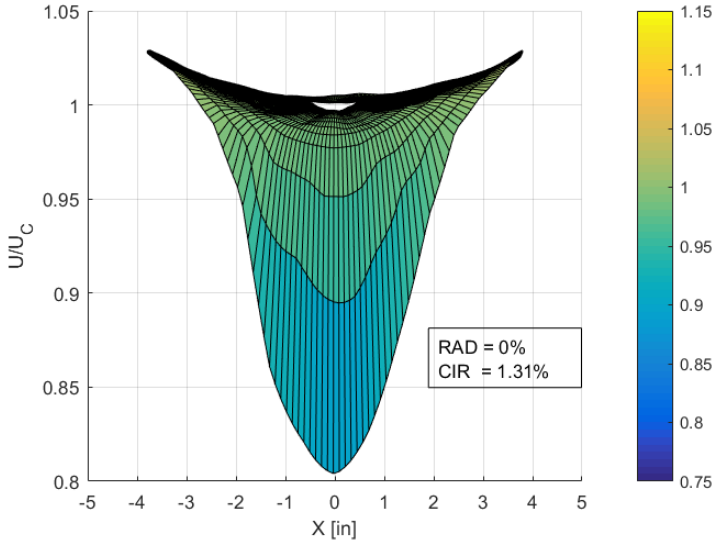

Figure 48: Lateral view of velocity contours for a 166 Hz pulsed plasma actuator at Configuration 1 and freestream velocity of 63 ft/s conditions.

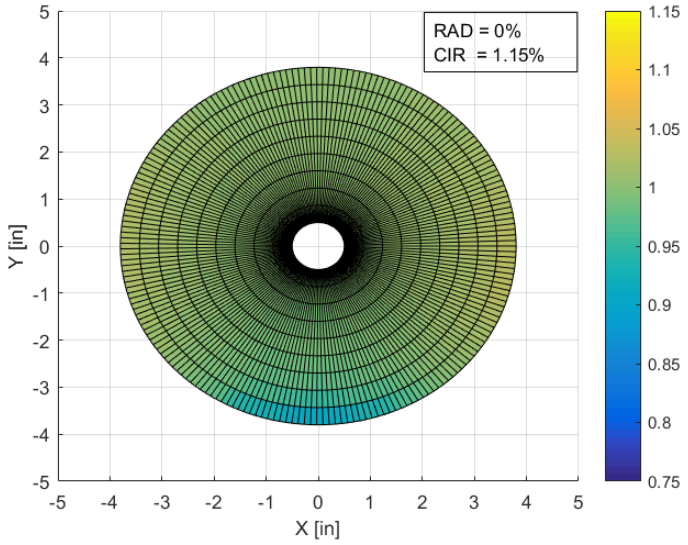

Figure 49: Velocity profile for a 10 Hz pulsed plasma actuator at Configuration 3 and freestream velocity of 63 ft/s condition.

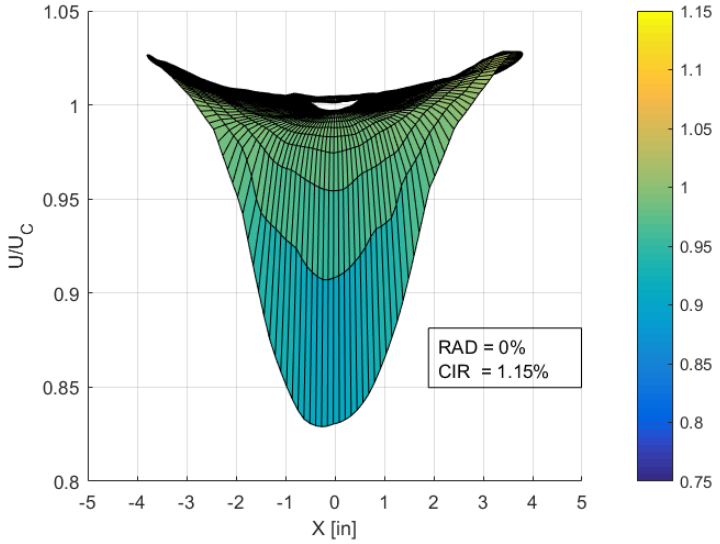

Figure 50: Lateral view of velocity contours for a 10 Hz pulsed plasma actuator at Configuration 3 and freestream velocity of 63 ft/s conditions.

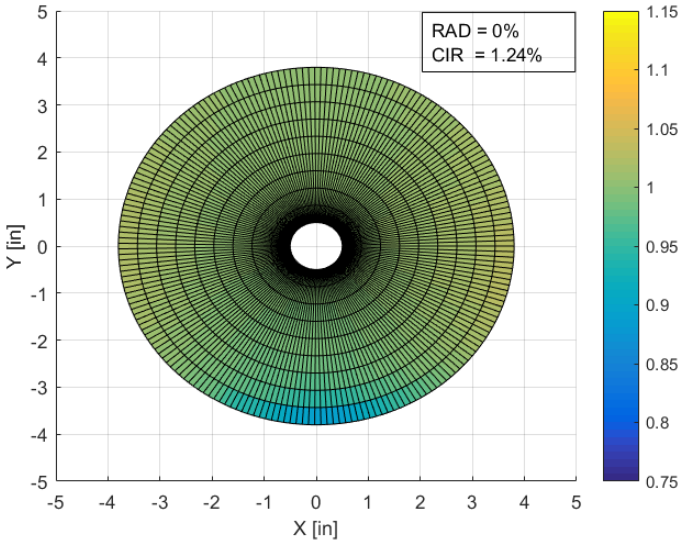

Figure 51: Velocity profile for a 100 Hz pulsed plasma actuator at Configuration 3 and freestream velocity of 63 ft/s condition.

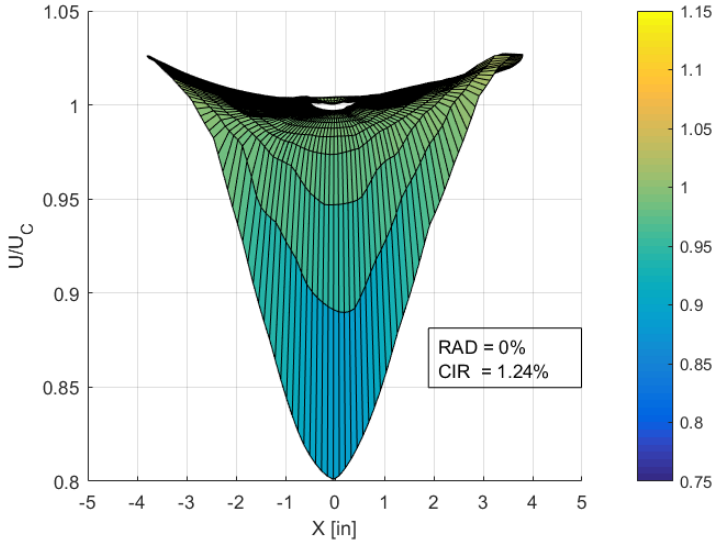

Figure 52: Lateral view of velocity contours for a 100 Hz pulsed plasma actuator at Configuration 3 and freestream velocity of 63 ft/s conditions.

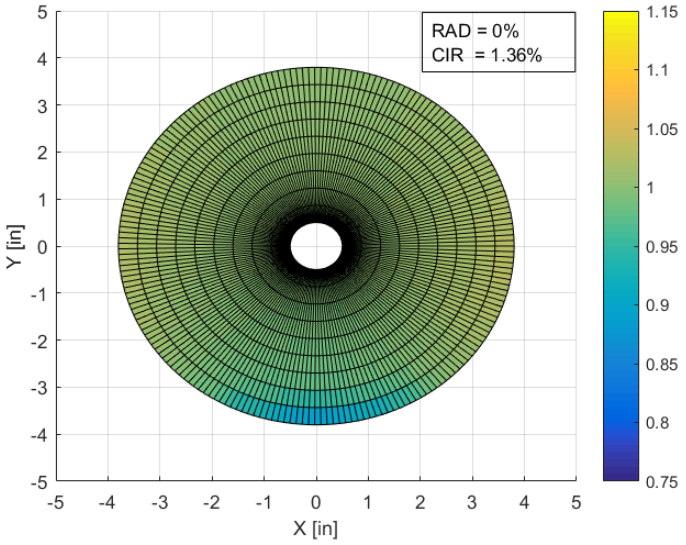

Figure 53: Velocity profile for a 166 Hz pulsed plasma actuator at Configuration 3 and freestream velocity of 63 ft/s condition.

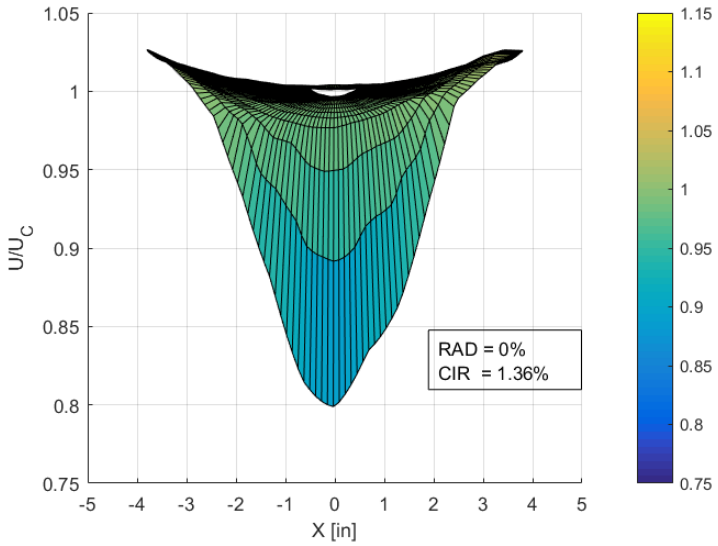

Figure 54: Lateral view of velocity contours for a 166 Hz pulsed plasma actuator at Configuration 3 and freestream velocity of 63 ft/s conditions.

Table 3: Experimental Results

Configuration	Wind Tunnel Speed	Plasma Operation	Frequency	$\Delta P_c/P$
Baseline	63 ft/s	Off	0 Hz	1.02%
Baseline	72 ft/s	Off	0 Hz	1.16%
Baseline	81 ft/s	Off	0 Hz	1.67%
1	63 ft/s	Off	0 Hz	1.26%
3	63 ft/s	Off	0 Hz	1.26%
1	63 ft/s	On	Continuous	1.29%
3	63 ft/s	On	Continuous	1.35%
1	63 ft/s	On	10 Hz	1.3%
3	63 ft/s	On	10 Hz	1.15%
1	63 ft/s	On	100 Hz	1.39%
3	63 ft/s	On	100 Hz	1.24%
1	63 ft/s	On	166 Hz	1.31%
3	63 ft/s	On	166 Hz	1.36%

CHAPTER V

UNCERTAINTY ANALYSIS

For this study, the Kline McClintock method is used for determining the uncertainty of values presented[61]. General equations used to determine overall uncertainty are shown below. The partial derivative numerator term shown in Equation 9 to calculate bias error corresponds to the parameter of interest. This will be V when determining bias error for wind tunnel freestream velocity and inlet duct centerline velocity. The partial derivative denominator term corresponds to the measurements taken to determine V, which are q, T and p. This weighting partial derivative, commonly referred to as the influence coefficient (I.C.), is multiplied by the bias, or precision error (b and p) of the instruments used in the experiments. Bias and precision of the parameter of interest (Bx and Px) are then calculated using this information. Equation 8 illustrates the overall uncertainty for a

Table 4: Uncertainty Analysis for Wind Tunnel Velocity

	Average Value	**Std. Dev.**	**I.C.**	**Bias**	**Precision**	**Total**
Temperature	520.8 R	12.2 R	0.051	0.51%	0.11%	0.52%
Pressure	2060.9 psf	16.9 psf	0.026	0.051%	0.014%	0.053%
Dynamic Pressure	4.55 psf	0.0146 psf	0.544	1.09%	0.03%	1.089%
Velocity	62.8 ft/s	0.20 ft/s		10.44%	0.018%	10.6%

measurement. Uncertainty was calculated for V_∞, and Table 4 illustrates the contributions of bias and precision to the overall uncertainty. Bias error for velocity was calculated using instrument bias error and the relative influence coefficient for each measurement. Precision error for velocity was determined using the mean and standard deviation of velocity measurements taken over the testing period. Bias error contributed to the majority of overall uncertainty for velocity, which is expected. Bias error may be reduced with more accurate instrumentation to improve the error associated, such as a high accuracy temperature probe. More tests could also be performed to reduce the precision error observed for this study.

$$B_x = \sqrt{(\frac{\partial X}{\partial y} \times b_y)^2 + (\frac{\partial X}{\partial z} \times b_z)^2 + ...} \tag{9}$$

$$P_x = \sqrt{(\frac{\partial X}{\partial y} \times p_y)^2 + (\frac{\partial X}{\partial z} \times p_z)^2 + ...} \tag{10}$$

$$U = \sqrt{B^2 + P^2} \tag{11}$$

CHAPTER VI

CONCLUSIONS

6.1. Conclusions from Experimental Results

A representative BLI arrangement was designed and manufactured to produce a distorted flow, and tests were conducted to characterize the arrangement prior to installing plasma actuators. Dynamic pressure measurements were used to calculate distortion intensities, which produced a dynamic circumferential distortion intensity of 1.02% at 63 ft/s. Increasing wind tunnel velocity to 72 ft/s produced a circumferential distortion intensity of 1.16%, and circumferential distortion intensity increased further to 1.67% at 81 ft/s. A trend was observed with increasing freestream velocity such that distortion intensity appears to increase with increasing wind tunnel velocity.

Multiple plasma flow control concepts were explored for manipulating distortion, and a SDBD plasma actuator was designed and manufactured for installation on the BLI arrangement. Two sizes of actuator were employed at various locations aft of the duct inlet lip to testing multiple variables.

An evaluation was then performed to determine the effectiveness of a plasma actuator to manipulate distortion in a representative BLI arrangement. Wind tunnel velocity, actuator location, and actuator frequency were varied to observe the effect on distortion intensity. The maximum and minimum actuator configurations were evaluated, Configu-

ration 1 at 1 inch aft and Configuration 3 at 5 inches aft of duct inlet. Dynamic pressure was used to calculate velocity in order to generate velocity profiles to qualitatively assess plasma actuator influence. Dynamic pressure measurements were used to calculate distortion intensities, which were reported for all tests.

Influence of attaching a plasma actuator to the surface at various locations was evaluated, and distortion intensity increased for Configuration 1 and 3 compared to the baseline case of no installed actuators. The increase in distortion due to actuator installation meant a new baseline case would need to be formed in order to properly evaluate the effect of plasma actuators during operation.

Finally, effectiveness of plasma actuators to manipulate distortion was evaluated for both steady and unsteady operation. Steady plasma operation results were inconclusive and did not reduce distortion intensity present. Next, unsteady operation was tested and multiple pulsed plasma actuator frequencies were evaluated to determine a corresponding effect on distortion intensity. Results for pulsing plasma at 100 and 166 Hz did not show a significant change in distortion intensity, increasing the magnitude for most cases. Furthermore, pulsing plasma at 10 Hz for Configuration 1 did not show a significant change in distortion intensity; however, at Configuration 3 the distortion intensity decreased by almost 9%. The reduction in distortion intensity at 10 Hz was the largest change witnessed for the conditions tested. The results of this study reveal the ability of plasma flow control to manipulate distortion intensity for an embedded duct arrangement.

6.2. Recommendations for Future Work

Many improvements and additional tests may be carried out to improve the quality and understanding of the effect of plasma actuators on manipulating distortion. First, higher resolution equipment in order to determine velocity direction and not only magnitude would significantly improve the understanding of the flow physics through the BLI arrangement. A two-axis hot wire probe would provide this capability and more accurately

resolve velocity fluctuation at the measurement plane.

Furthermore, machining actuators as opposed to hand making each one would decrease the variation between multiple assemblies, and embedding the actuators into the BLI arrangement would reduce the variability associated with tripping the flow upstream of the measurement probe.

Additionally, several more tests could be performed to more thoroughly evaluate plasma actuator effectiveness. Further work could be performed to observe an optimal plasma actuator location, as well as an optimal plasma pulsing frequency to enhance effectiveness at manipulating distortion. With this information, a more thorough understanding of plasma actuator effect on distorted flow through an embedded duct would be accomplished.

REFERENCES

[1] Plas, A., Crichton, D., Sargeant, M., Hynes, T., Greitzer, E., Hall, C., and Madani, V., "Performance of a boundary layer ingesting (BLI) propulsion system," *45th AIAA aerospace sciences meeting and exhibit*, 2007, p. 450.

[2] Uranga, A., Drela, M., Greitzer, E., Titchener, N., Lieu, M., Siu, N., Huang, A., Gatlin, G. M., and Hannon, J., "Preliminary Experimental Assessment of the Boundary Layer Ingestion Benefit for the D8 Aircraft," *52nd Aerospace Sciences Meeting*, 2014, p. 0906.

[3] Roth, J., Sherman, D., and Wilkinson, S., "Boundary layer flow control with a one atmosphere uniform glow discharge surface plasma," *36th AIAA Aerospace Sciences Meeting and Exhibit*, 1998, p. 328.

[4] Corke, T. C., Enloe, C. L., and Wilkinson, S. P., "Dielectric barrier discharge plasma actuators for flow control," *Annual review of fluid mechanics*, Vol. 42, 2010, pp. 505–529.

[5] Drela, M., "Power balance in aerodynamic flows," *AIAA journal*, Vol. 47, No. 7, 2009, pp. 1761–1771.

[6] Drela, M., "Development of the D8 transport configuration," *29th AIAA Applied Aerodynamics Conference*, 2011, p. 3970.

[7] Smith, L. H., "Wake ingestion propulsion benefit," *Journal of Propulsion and Power*, Vol. 9, No. 1, 1993, pp. 74–82.

[8] Geiselhart, K. A., Daggett, D. L., Kawai, R., and Friedman, D., "Blended wing body systems studies: boundary layer ingestion inlets with active flow control," 2003.

[9] Kawai, R. T., Friedman, D. M., and Serrano, L., "Blended Wing Body (BWB) Boundary Layer Ingestion (BLI) Inlet Configuration and System Studies," 2006.

[10] Liebeck, R. H., "Design of the blended wing body subsonic transport," *Journal of aircraft*, Vol. 41, No. 1, 2004, pp. 10–25.

[11] Greitzer, E., Bonnefoy, P., Blanco, E. l. R., Dorbian, C., Drela, M., Hall, D., Hansman, R., Hileman, J., Liebeck, R., Lovegren, J., et al., "N+ 3 aircraft concept designs and trade studies, final report volumes 1 and 2," *Rep. CR2010-216794, NASA, Hampton, VA*, 2010.

[12] Hileman, J., Spakovszky, Z., Drela, M., Sargeant, M., and Jones, A., "Airframe design for silent fuel-efficient aircraft," *Journal of aircraft*, Vol. 47, No. 3, 2010, pp. 956–969.

[13] NASA, "Boundary Layer Ingestion Propulsion," , 2018. URL `https://www1.grc.nasa.gov/aeronautics/bli`.

[14] White, F., *Viscous Fluid Flow*, McGraw-Hill series in mechanical engineering, McGraw-Hill, 1991. URL `https://books.google.com/books?id=G6IeAQAAIAAJ`.

[15] Schlichting, H., and Kestin, J., *Boundary layer theory*, McGraw-Hill series in mechanical engineering, McGraw-Hill, 1960. URL `https://books.google.com/books?id=gtXjoAEACAAJ`.

[16] Zhang, Q., "Laminar-turbulent transition for attached and separated flow," 2010.

[17] Chue, R., Hynes, T., Greitzer, E., Tan, C., and Longley, J., "Calculations of inlet distortion induced compressor flow field instability," *International Journal of Heat and Fluid Flow*, Vol. 10, No. 3, 1989, pp. 211–223.

[18] Longley, J. P., "Inlet distortion and compressor stability." Ph.D. thesis, University of Cambridge, 1988.

[19] Longley, J., and Greitzer, E., "Inlet distortion effects in aircraft propulsion system integration," 1992.

[20] Fidalgo, V. J., Hall, C., and Colin, Y., "A study of fan-distortion interaction within the nasa rotor 67 transonic stage," *Journal of Turbomachinery*, Vol. 134, No. 5, 2012, p. 051011.

[21] Liu, H., Wang, Y., Xian, S., and Hu, W., "Effect of inlet distortion on the performance of axial transonic contra-rotating compressor," *Proceedings of the Institution of Mechanical Engineers, Part G: Journal of Aerospace Engineering*, Vol. 232, No. 1, 2018, pp. 42–54.

[22] Cousins, W. T., "History, philosophy, physics, and future directions of aircraft propulsion system/inlet integration," *ASME Turbo Expo 2004: Power for Land, Sea, and Air*, American Society of Mechanical Engineers, 2004, pp. 305–320.

[23] Cousins, W. T., Voytovych, D., Tillman, G., and Gray, E., "Design of a Distortion-Tolerant Fan for a Boundary-Layer Ingesting Embedded Engine Application," *53rd AIAA/SAE/ASEE Joint Propulsion Conference*, 2017, p. 5042.

[24] Bloch, G. S., "An Assessment of Inlet Total-Pressure Distortion Requirements for the Compressor Research Facility (CRF)," Tech. rep., WRIGHT LAB WRIGHT-PATTERSON AFB OH AERO PROPULSION AND POWER DIRECTORATE, 1992.

[25] Hoopes, K. M., "A new method for generating swirl inlet distortion for jet engine research," Ph.D. thesis, Virginia Tech, 2013.

[26] Hermanson, K. S., and Thole, K. A., "Effect of inlet conditions on endwall secondary flows," *Journal of Propulsion and Power*, Vol. 16, No. 2, 2000, pp. 286–296.

[27] Praisner, T., and Smith, C., "The Dynamics of the Horseshoe Vortex and Associated Endwall Heat TransferPart I: Temporal Behavior," *Journal of Turbomachinery*, Vol. 128, No. 4, 2006, pp. 747–754.

[28] Praisner, T., and Smith, C., "The dynamics of the horseshoe vortex and associated endwall heat transferpart ii: Time-mean results," *Journal of Turbomachinery*, Vol. 128, No. 4, 2006, pp. 755–762.

[29] Gad-el Hak, M., "Flow control," *Applied mechanics reviews*, Vol. 42, No. 10, 1989, pp. 261–293.

[30] Corporation, T., "Titleist Pro-V1 Golf Balls," , 1999. URL `https://www.titleist.com/golf-balls/pro-v1-pro-v1x`.

[31] Volino, R. J., "Passive flow control on low-pressure turbine airfoils," *ASME Turbo Expo 2003, collocated with the 2003 International Joint Power Generation Conference*, American Society of Mechanical Engineers, 2003, pp. 833–844.

[32] Shun, S., and Ahmed, N., "Wind turbine performance improvements using active flow control techniques," *Procedia engineering*, Vol. 49, 2012, pp. 83–91.

[33] Kale, N. V., *Active and hybrid flow control in s-ducts and diffusers*, University of Illinois at Urbana-Champaign, 2013.

[34] Bons, J. P., Sondergaard, R., and Rivir, R. B., "Turbine separation control using pulsed vortex generator jets," *ASME Turbo Expo 2000: Power for Land, Sea, and Air*, American Society of Mechanical Engineers, 2000, pp. V003T01A067–V003T01A067.

[35] Zhang, X. F., and Hodson, H., "Combined effects of surface trips and unsteady wakes on the boundary layer development of an ultra-high-lift LP turbine blade," *Journal of Turbomachinery*, Vol. 127, No. 3, 2005, pp. 479–488.

[36] Zhang, X. F., Vera, M., Hodson, H., and Harvey, N., "Separation and transition control on an aft-loaded ultra-high-lift LP turbine blade at low Reynolds numbers: low-speed investigation," *Journal of Turbomachinery*, Vol. 128, No. 3, 2006, pp. 517–527.

[37] Lin, J., Howard, F., Bushnell, D., and Selby, G., "Investigation of several passive and active methods for turbulent flow separation control," *21st Fluid Dynamics, Plasma Dynamics and Lasers Conference*, 1990, p. 1598.

[38] Chang, P. K., *Separation of flow*, Elsevier, 2014.

[39] Gamerdinger, P. M., "The Effects of Low-Profile Vortex Generators on Flow in a Transonic Fan-Blade Cascade." Tech. rep., NAVAL POSTGRADUATE SCHOOL MONTEREY CA, 1995.

[40] Rao, D., and Kariya, T., "Boundary-layer submerged vortex generators for separation control-an exploratory study," *1st National Fluid Dynamics Conference*, 1988, p. 3546.

[41] NEUMANN, H., POVINELLI, L., and COLTRIN, R., "An analytical and experimental study of a short S-shaped subsonic diffuser of a supersonic inlet," *18th Aerospace Sciences Meeting*, 1980, p. 386.

[42] Stumpf, R., NEUMANN, H., and GIAMATI, C., "Dynamic distortion in a short s-shaped subsonic diffuser with flow separation," *19th Joint Propulsion Conference*, ????, p. 1412.

[43] McAuliffe, B. R., and Sjolander, S. A., "Active flow control using steady blowing for a low-pressure turbine cascade," *ASME Turbo Expo 2004: Power for Land, Sea, and Air*, American Society of Mechanical Engineers, 2004, pp. 1223–1235.

[44] Seifert, A., Bachar, T., Koss, D., Shepshelovich, M., and Wygnanskil, I., "Oscillatory blowing: a tool to delay boundary-layer separation," *AIAA journal*, Vol. 31, No. 11, 1993, pp. 2052–2060.

[45] Harper, D., Leitch, T., Ng, W., Guillot, S., and Burdisso, R., "Boundary layer control and wall-pressure fluctuations in a serpentine inlet," *36th AIAA/ASME/SAE/ASEE Joint Propulsion Conference and Exhibit*, 2000, p. 3597.

[46] Hamstra, J., Miller, D., Truax, P., Anderson, B., and Wendt, B., "Active inlet flow control technology demonstration," *The Aeronautical Journal*, Vol. 104, No. 1040, 2000, pp. 473–479.

[47] Gorton, S., Owens, L., Jenkins, L., Allan, B., and Schuster, E., "Active flow control on a boundary-layer-ingesting inlet," *42nd AIAA Aerospace Sciences Meeting and Exhibit*, 2004, p. 1203.

[48] Jenkins, L. N., Gorton, S. A., and Anders, S. G., "Flow control device evaluation for an internal flow with an adverse pressure gradient," 2002.

[49] Bittencourt, J. A., *Fundamentals of plasma physics*, Springer Science & Business Media, 2013.

[50] Roth, J. R., Sherman, D. M., and Wilkinson, S. P., "Electrohydrodynamic flow control with a glow-discharge surface plasma," *AIAA journal*, Vol. 38, No. 7, 2000, pp. 1166–1172.

[51] Narayanaswamy, V., Shin, J., Clemens, N., and Raja, L., "Investigation of plasma-generated jets for supersonic flow control," *46th AIAA Aerospace Sciences Meeting and Exhibit*, 2008, p. 285.

[52] Narayanaswamy, V., Raja, L. L., and Clemens, N. T., "Characterization of a high-frequency pulsed-plasma jet actuator for supersonic flow control," *AIAA journal*, Vol. 48, No. 2, 2010, pp. 297–305.

[53] Narayanaswamy, V., Raja, L. L., and Clemens, N. T., "Control of a shock/boundary-layer interaction by using a pulsed-plasma jet actuator," *AIAA journal*, Vol. 50, No. 1, 2012, pp. 246–249.

[54] Utkin, Y. G., Keshav, S., Kim, J.-H., Kastner, J., Adamovich, I. V., and Samimy, M., "Development and use of localized arc filament plasma actuators for high-speed flow control," *Journal of Physics D: Applied Physics*, Vol. 40, No. 3, 2006, p. 685.

[55] Samimy, M., Adamovich, I., Webb, B., Kastner, J., Hileman, J., and Palm, P., "Development and application of localized arc filament plasma actuators for jet flow and noise control," *42nd AIAA Aerospace Sciences Meeting and Exhibit*, 2004, p. 184.

[56] Corke, T., Jumper, E., Post, M., Orlov, D., and McLaughlin, T., "Application of weakly-ionized plasmas as wing flow-control devices," *40th AIAA Aerospace Sciences Meeting & Exhibit*, 2002, p. 350.

[57] Huang, J., Corke, T. C., and Thomas, F. O., "Unsteady plasma actuators for separation control of low-pressure turbine blades," *AIAA journal*, Vol. 44, No. 7, 2006, pp. 1477–1487.

[58] Thomas, F. O., Kozlov, A., and Corke, T. C., "Plasma actuators for cylinder flow control and noise reduction," *AIAA journal*, Vol. 46, No. 8, 2008, pp. 1921–1931.

[59] Mattingly, J. D., Boyer, K. M., and von Ohain, H., *Elements of propulsion: gas turbines and rockets*, American Institute of Aeronautics and Astronautics Reston, Virginia, 2006.

[60] Berrier, B. L., and Morehouse, M. B., "Evaluation of flush-mounted, s-duct inlets with large amounts of boundary layer ingestion," 2003.

[61] Kline, S. a., and McClintock, F., "A., 1953,Describing Uncertainties in Single-Sample Experiments, ASME Mech," *Eng*, Vol. 75, ????, pp. 3–8.

VITA

Tyler Zimbelman

Candidate for the Degree of

Master of Science

Thesis: PLASMA FLOW CONTROL FOR
DISTORTION TOLERANT FANS WITH AIRCRAFT
BOUNDARY LAYER INGESTION

Major Field: Mechanical and Aerospace Engineering

Biographical:

Education:

Completed the requirements for the Master of Science in Mechanical and Aerospace Engineering at Oklahoma State University, Stillwater, Oklahoma in May, 2018.

Completed the requirements for the Bachelor of Science in Biosystems Engineering at Oklahoma State University, Stillwater, Oklahoma in May, 2013.

Experience:

Mechanical Engineer at Thru Tubing Solutions, Oklahoma City, Oklahoma
Project Engineer at Zeeco, Broken Arrow, Oklahoma